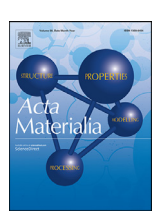


Contents lists available at ScienceDirect

Acta Materialia

journal homepage: www.elsevier.com/locate/actamat



Elucidating the temperature dependence of TRIP in Q&P steels using synchrotron X-Ray diffraction, constituent phase properties, and strain-based kinetics models



Christopher B. Finfrock^{a,*}, Benjamin Ellyson^a, Sri Ranga Jai Likith^a, Douglas Smith^a, Connor J. Rietema^{a,b}, Alec I. Saville^a, Melissa M. Thrun^a, C. Gus Becker^a, Ana L. Araujo^c, Erik J. Pavlina^d, Jun Hu^e, Jun-Sang Park^f, Amy J. Clarke^a, Kester D. Clarke^a

- ^a Colorado School of Mines, 1500 Illinois St., Golden, 80401, CO, USA
- ^b Lawrence Livermore National Laboratory, 7000 East Ave, Livermore, 94550, CA, USA
- ^c CBMM North America, Inc., 1000 Omega Dr., Pittsburgh, 15205, PA, USA
- ^d Stress Engineering Services, Inc., 7030 Stress Engineering Way, Mason, 45040, OH, USA
- e Cleveland-Cliffs, Inc., 6180 Research Way, Middletown, 45005, OH, USA
- ^f Argonne National Laboratory, 9700 S. Cass Avenue, Lemont, 60439, IL, USA

ARTICLE INFO

Article history: Received 21 March 2022 Revised 24 May 2022 Accepted 23 June 2022 Available online 1 July 2022

Keywords:

High energy X-ray diffraction Transformation-induced plasticity Martensitic phase transformation Quenching and partitioning Advanced high strength steels

ABSTRACT

Understanding the deformation-induced martensitic transformation (DIMT) is critical for interpreting the structure-property relationships that govern the performance of transformation-induced plasticity (TRIP) assisted steels. However, modern TRIP-assisted steels often exhibit DIMT kinetics that are not easily captured by existing empirical models based on bulk tensile strain. We address this challenge by combined bulk uniaxial tensile tests and *in-situ* high energy synchrotron X-ray diffraction, which resolved the phase volume fractions, stress-strain response, and microstructure evolution of each constituent phase. A modification of the Olson-Cohen model is implemented, which describes the martensitic transformation kinetics as a function of the estimated partitioned strain in austenite, rather than the bulk tensile strain. This DIMT kinetic model is used as a framework to clarify the root cause of an insufficiently understood toughness trough reported for TRIP-assisted steels during deformation at elevated temperatures. The importance of the temperature-dependent toughness is discussed, based on the opportunity to modify deformation processes to tailor the DIMT kinetics and mechanical properties during forming and in service.

© 2022 Acta Materialia Inc. Published by Elsevier Ltd. All rights reserved.

1. Introduction

Martensitic phase transformations are increasingly utilized to obtain enhanced mechanical property combinations in engineered materials, particularly under severe deformation conditions. Possibilities for toughness enhancements have been identified for several material classes, including zirconia ceramics [1], high entropy alloys [2–4], titanium alloys [5,6], and advanced high strength steels (AHSS) [7,8]. The transformation-induced plasticity (TRIP) effect is thought to be the principal mechanism by which martensitic phase transformations strengthen such materials. For instance, in blast and penetration resistant steels for protective structures, the TRIP effect is known to suppress plastic instability and shear band-

E-mail address: cfinfroc@mines.edu (C.B. Finfrock).

ing [9]. Meanwhile, in steels designed for automotive crash structures, the TRIP effect is used to enhance the formability and toughness [7]

In AHSS, the TRIP effect increases formability by several mechanisms. First, dislocations are generated during the deformation-induced martensitic transformation (DIMT) to maintain plastic compatibility between constituents (e.g., at austenite-martensite interfaces), which results in strain hardening. Second, depending on the strain state, the volume expansion associated with DIMT can provide an additional pathway for strain accommodation. Third, constituent phases in AHSS offer distinctive properties, and the phases deform in a composite manner within the bulk. For example, ferrite is soft and ductile, while martensite and metastable austenite are hard [10]. As a result, bulk property combinations can be tailored by adjusting the individual-phase properties and the fractions of each constituent. During DIMT in Quenching and Partitioning (Q&P) steels, new/untempered martensite pro-

^{*} Corresponding author.

Table 1
Common Strain-Based Models for DIMT.

Equation	Reference
$f_{\varepsilon}^{\gamma} = f_{\varepsilon}^{\gamma=0} [1 - exp(-\beta[1 - exp(-\alpha\varepsilon)]^n)]$ $f_{\varepsilon}^{\gamma} = f_{\varepsilon}^{\gamma=0}/(1 + p/[k\varepsilon f_{\varepsilon}^{\gamma=0}])$	Olson-Cohen (OC) [30] Burke-Matsumura (BM) [44.45]

 $f_{\varepsilon=0}^{\gamma}=$ Austenite content before deformation. $f_{\varepsilon}^{\gamma}=$ Austenite content after deformation.

gressively forms at the expense of austenite, which increases the bulk strength because untempered martensite is approximately 30 pct. harder than austenite [10]. Although it is understood that constituent phase properties are critical for tuning and maximizing property combinations, it is difficult to measure them during bulk mechanical testing. For instance, individual-phase stresses are relieved upon unloading, so it is impossible to measure such values with common *ex-situ* tools. Bulk *in-situ* characterization techniques have emerged to solve this problem; they can show how complex microstructures accommodate strain with a combination of dislocation slip and TRIP. In particular, high energy X-ray diffraction (HEXRD) using a synchrotron source can provide outstanding spatial and temporal resolution of the phase volume fraction [11], plastic strain accumulation [12], and elastic stresses for each constituent phase [13] during bulk mechanical testing.

The concept of austenite stability has been used to describe the kinetics of DIMT as a function of the applied strain [14,15]; less stable refers to austenite which undergoes DIMT more rapidly. The study of austenite stability is of topical interest to enhance the properties of TRIP-assisted steels, because austenite stability decisively influences properties during forming and in service [8]. Strain-based models for DIMT have been proposed in the literature, such as the Olson-Cohen (OC) and Burke-Matsumura (BM) models (see Table 1). A review of the relevant models is provided by Samek et al. [14]. Generally, these empirically-derived models correctly capture the DIMT kinetics in fully austenitic steels, where the austenite grains are relatively chemically and morphologically homogeneous. However, the models struggle to capture the DIMT kinetics of steels with complex microstructures, where austenite grains exist with a spectrum of compositions, sizes, and shapes, and strain is partitioned unevenly between the constituent phases.

The complexity of austenite stability in multi-phase steels has motivated targeted efforts within the literature. Recently, He divided the factors that influence the stability of austenite into "intrinsic" or "extrinsic" with respect to an individual austenite grain [16]. Intrinsic factors include dislocation density [17], alloy partitioning, and the composition, morphology, size, and orientation of austenite [18]. Extrinsic factors include strain rate [19-21], temperature [22–25], strain state [26,27], and surrounding microstructure [28]. Increasing the deformation temperature decreases the chemical driving force for DIMT, which is represented by the austenite stability parameters, k and β , in the BM and OC models, respectively. For Q&P steels, Poling et al. and Feng et al. showed that β decreased with increasing deformation temperature up to 100 °C [22,23], thereby suppressing DIMT kinetics. Temperature can also influence the austenite stacking fault energy, which can affect the formation of shear band intersections, the primary sites for martensite embryo nucleation [29]. In the OC model, a martensite nucleation parameter, α , is used to capture this phenomenon. For fully austenitic steels, Olson and Cohen showed that α decreased with increasing temperature [30], while a similar trend was shown for Q&P steels up to 100 °C by Poling et al. [22]. Strain rate is of particular importance, because stamping operations and vehicle crashes generally impart deformation at high enough strain rates to raise sheet temperatures on the order of 50 to 100 °C above-ambient conditions [31,32]. For reference, sheet forming and vehicle crashes impart strain rates from 10^{-1} to $10 \, s^{-1}$ and 10^2 to $10^3 \, s^{-1}$, respectively [33–35]. Furthermore, in previous work by the authors, it was shown that strain rate exhibited an independent effect on DIMT kinetics that was not attributed to adiabatic heating, over a range of 10^{-4} to $10^{-1} \, s^{-1}$ [19,36,37]. Rather, an acceleration of DIMT was observed, likely due to a positive correlation between the strain rate and the number of stacking fault intersections that were available to nucleate martensite, along with higher stresses on the austenite [19,36].

A source of inaccuracy in the empirical models for DIMT is that austenite stability is linked not only to the properties of the austenite (e.g., composition, size, and morphology), but also the properties of the surrounding phases within the microstructure. For instance, the flow stress of body centered cubic (BCC) crystal structures, that is, of ferrite, bainite, and martensite, is known to be strongly temperature and strain rate sensitive because of the thermal activation of dislocation slip in BCC crystal structures [38]. Because dislocation slip activation is less temperature sensitive in face centered cubic (FCC) crystal structures [38], (for example, in austenite,) there exists the possibility of variations in stress partitioning as a function of temperature and bulk strain. Furthermore, dynamic strain aging, dislocation recovery, or tempering of martensite or bainite at elevated temperatures could also influence the stress partitioning between phases [39], leading to different effective stresses and strains in the austenite. Recently, as strainbased DIMT models have been applied to complex phase alloys, it has been reported that the partitioned strain of austenite should be used rather than the bulk strain [40,41]. However, from an experimental perspective, measuring the partitioned strain of austenite is a significant technical challenge. This capability is under development both on the microstructure-scale using electron backscatter diffraction digital image correlation (EBSD-DIC) [42] and on the bulk-scale using neutron or X-ray diffraction [43].

Several recent studies have aimed to resolve how the balance of dislocation slip and TRIP influences the mechanical properties of AHSS, while considering strain rate and temperature. For instance, Liu et al. and Finfrock et al. both observed that inhibited DIMT kinetics led to a ductility trough at strain rates around 10^{-1} s⁻¹ at 25 °C [19,46]. Likewise, Coryell et al. discovered an analogous ductility trough for tensile tests at various temperatures under quasistatic strain rates. In Coryell's work, a minimum ductility at 100 °C coincided with the suppression of DIMT and a high local lattice misorientation, which was attributed to strain accommodation primarily via dislocation slip [24]. The governing mechanism for both effects may be related; for instance, Frint et al. observed that the strain rate sensitivity of ductility was promoted at elevated temperatures [47]. Previous work has not established a clear explanation for the behavior based solely on the chemical stability of austenite [19,24,46,47]. Fortunately, temperature can be adjusted during sheet metal forming with die heating or cooling. Likewise, strain rate can be adjusted during forming by manipulating forming press speeds. Thus, if the root cause(s) of the temperature and strain rate dependent ductility troughs can be established, there exists a possibility to modify deformation processes for improved mechanical response during forming and performance in service.

Here, we resolve the individual-phase deformation responses and DIMT kinetics for several Q&P steels with different microstructures, along with a dual phase (DP) steel to serve as a baseline for properties in the absence of austenite. Bulk mechanical testing at ambient and above-ambient temperatures, along with *in-situ* HEXRD data, are combined with post-mortem spatially-resolved electron backscatter diffraction (EBSD) to elucidate a stress partitioning mechanism that strongly impacts DIMT kinetics and TRIP strengthening. For the first time, stress partitioning, considered in combination with the traditional understanding of the chem-

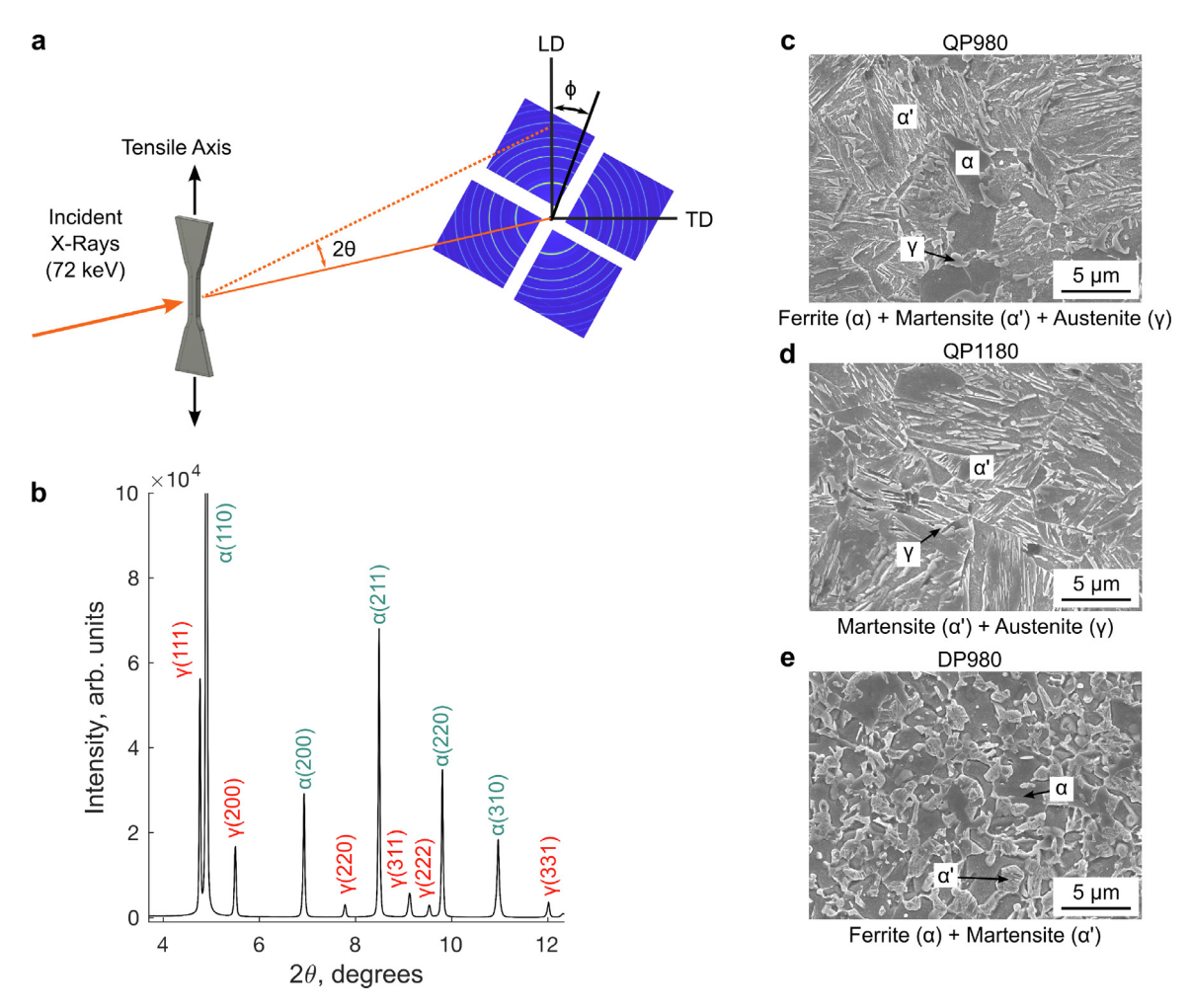


Fig. 1. (a) Schematic of the high-energy X-ray diffraction (HEXRD) geometry at the 1-ID beamline at the Advanced Photon Source. Debye-Scherrer rings are shown for the DP980 steel prior to deformation. (b) Example of a one-dimensional lineout for the QP980 steel. The lineouts were created by integrating around the azimuthal angle (ϕ) using GSAS-II software. Note that to show the high signal-to-noise ratio of the low intensity reflections, the full height of the α (110) reflection is not shown in (b). (c-e) Normal-direction SEM micrographs of QP980, QP1180, and DP980, respectively. The rolling and loading direction are to the right in the micrographs.

ical stability and martensitic embryo nucleation, is proposed as a principal mechanism by which a DIMT trough exists at above-ambient temperatures in Q&P steels. Furthermore, dislocation density measurements in the BCC phases are used to relate the DIMT kinetics to the ductility trough [19,24,46,47]. The concurrent implementation of diffraction tools along multiple length scales (from sub- μm to mm) revealed insights about stress partitioning and TRIP kinetics that have been impossible to reach using ex-situ tests alone.

2. Experimental procedure

Bulk tensile tests at various temperatures were conducted with *in-situ* HEXRD at the 1-ID beamline at the Advanced Photon Source (APS) at Argonne National Laboratory. The tests elucidated the roles of temperature and microstructure on deformation in several advanced high strength steels (AHSS). Using the *in-situ* HEXRD technique (Fig. 1(a,b)), we coupled bulk mechanical testing data with high-temporal resolution measurements of the tensile stresses, strains, and volume fractions of individual constituent phases. Subsequently, we augmented the HEXRD and mechanical testing data with spatially-resolved *ex-situ* EBSD maps, to clarify how local lattice rotation and crystallographic texture was correlated to bulk properties.

2.1. Experimental materials

Three commercially-available lean-alloy AHSS were provided by Cleveland Cliffs Steel Corporation: QP980, QP1180, and DP980. The steels were fully finished on an industrial mill. First, the steels were hot rolled, coiled, cooled, then cold rolled to a nominal 50 percent thickness reduction [37]. Subsequently, the steels were heat treated and hot-dip galvannealed. Each steel was manufactured using distinctive alloy contents and heat treatment schedules, which were intended to generate different property combinations by tuning the microstructure, phase constituents, and strengthening mechanisms. The steels are named based on the heat treatment approach used; "QP" and "DP" refer to "quenching and partitioning" and "dual phase", respectively. The steels are also named based on their intended minimum ultimate tensile strength (that is, 980 and 1180 MPa). The thicknesses of QP980, QP1180, and DP980 are 1.0, 1.0, and 1.4 mm, respectively.

The chemical composition of each steel was determined with a combination of several analytical techniques including inert gas fusion, combustion, and inductively coupled plasma mass spectrometry. The chemical compositions are shown in Table 2. The two Q&P steels contain additions of C and Mn for increasing the stability of austenite and the hardenability, as well as Si which is known to suppress the formation of carbides that could deleteriously limit the amount of carbon that partitions to austenite. The

Acta Materialia 237 (2022) 118126

 Table 2

 Compositions and Phase Fractions of the Experimental Steels.

Steel	C wt pct	Mn wt pct	Si wt pct	Cr wt pct	Mo wt pct	Austenite vol pct	Ferrite vol pct
QP980	0.20	1.96	1.68	0.03	< 0.02	11.2	26
QP1180	0.19	2.31	1.64	0.02	< 0.02	10.7	0
DP980	0.09	0.23	0.12	0.58	0.10	<1	42

carbon content of austenite (C_{γ}) was estimated using HEXRD to be 1.16 and 1.13 wt percent for QP980 and QP1180 (see Appendix A for details). In QP980, it was assumed that equilibrium partitioning of manganese to austenite occurred during intercritical annealing, leading to an estimated nominal austenite manganese content of 2.65 wt pct. However, it is noted that the assumption of equilibrium manganese partitioning was not validated experimentally. Meanwhile, the DP980 contained a lower amount of C, Mn, and Si, as well as additions of Cr and Mo for hardenability enhancements.

Representative SEM micrographs of each steel etched with one pct. Nital are shown in Fig. 1(c-e). QP980 contained \sim 26 vol. pct. ferrite (α) formed during an intercritical annealing step. During a subsequent quenching and partitioning process, \sim 12 vol. pct. austenite (γ) was retained, with the remainder being a mix of tempered and untempered martensite (α '). The QP1180 was fully austenitized, and so the microstructure did not contain substantial amounts of ferrite. The QP1180 also retained \sim 12 vol. pct. austenite during Q&P processing, with the remainder martensite. By a combination of SEM secondary electron imaging and EBSD mapping, the austenite particles appeared to be similar in size and morphology between QP980 and QP1180. Both steels exhibited austenite particles with a range of aspect ratios, and the average austenite particle size for both steels was approximately 1-2 µm. One caveat with this analysis is that EBSD lacks the spatial resolution to detect very fine austenite particles. The DP980 steel exhibited a ferrite-based microstructure with dispersed islands of martensite and negligible austenite (i.e., f_{γ} <1 vol. pct.). Each steel was observed to contain a comparably refined prior austenite structure, and the structure was further-refined during the formation of the martensitic matrix. The intercritically-annealed steels, QP980 and DP980, exhibited ferrite grain diameters of approximately 5 and 2 µm, respectively. The approximate volume fraction of intercritical ferrite and austenite in each steel is listed in Table 2, with the balance being martensite.

2.2. Mechanical testing

Tensile specimens of each steel were machined with the loading direction (LD) parallel to the rolling direction (RD) of the sheets. The gauge sections of the specimens were 6 mm long and 1.4 mm wide. The as-received sheet thickness was used. Before testing at the APS, the Zn-coating was chemically removed with a mixture of 20 pct. hydrochloric acid, 30 pct. hydrogen peroxide, and 50 pct. water.

An MTS servo-hydraulic load frame was used to monotonically load each specimen until fracture in uniaxial tension, using a nominal engineering strain rate of $2 \times 10^{-4} \ s^{-1}$. A load cell was used to determine the stress. Crosshead displacement was used to calculate strain, and elastic deflection in the frame was removed from the crosshead displacement using the reciprocal springs-in-series relationship. After calculating true stress (σ) and true strain (ε) , Eq. (1) was used to calculate the instantaneous strain hardening exponent (n_i) [48]:

$$n_i = \frac{d(\ln \sigma)}{d(\ln \varepsilon)} \tag{1}$$

Where n_i is a representation of the work hardening within the steel that can be directly related to the rate of strain hardening $(\frac{d\sigma}{d\epsilon})$ [48]:

$$\frac{d\sigma}{d\varepsilon} = n\frac{\sigma}{\varepsilon} \tag{2}$$

Specimens were deformed at temperatures of 25, 100, 175, and 250 °C. An infrared furnace was used to heat the specimens over a period of \sim 5 min. The furnace temperature was controlled using a K-type thermocouple attached directly to the gauge section of each sample. Only one specimen of each material and temperature was tested. Trends in the mechanical testing and phase volume fraction evolution as a function of steel and temperature were verified externally in separate tensile tests.

2.3. In-situ high energy X-ray diffraction (HEXRD)

2.3.1. HEXRD experimental configuration

Haas et al. and Zhang et al. provided a comprehensive overview of the wide angle X-ray scattering diffraction configuration at the 1-ID beamline at APS [49,50]. For this experiment, a monochromatic beam of X-rays at an energy of 71.68 keV ($\lambda = 0.1731 \text{ Å}$) with a cross section of 130 \times 130 μm was used. The beam transmitted through the center of the gauge section of the specimens, with the beam propagation direction normal to the plane of the sheet. Considering the fine grain structure of each steel and the large beam interaction volume, i.e., the beam cross section times the sheet thickness, the synchrotron beam interacted with hundreds of thousands of individual grains. Debye-Scherrer rings were detected using the "Hydra" detector array, which was composed of four GE Angio area detectors [51]. Each detector in the array was arranged to capture diffracted rings from either the LD or transverse direction (TD) of the tensile specimen. Figure 1(a) shows a schematic of the in-situ HEXRD geometry. HEXRD data were captured prior to and throughout deformation to fracture. However, to isolate the moments where strain was nominally homogeneous, only the data collected up to the end of uniform elongation are presented here.

2.3.2. HEXRD line profile analysis

The GSAS-II software package was used to reduce the twodimensional data from each detector into one-dimensional "lineouts" [52]. First, the position of each area detector was calibrated using CeO₂ (NIST SRM 674b). Next, the intensity data from each detector were radially integrated. Two sets of integration parameters were used for determining (i) phase volume fractions and (ii) stresses on individual-phase constituents. For (i), all four detectors were integrated over a scattering vector (i.e., $Q = 4\pi \sin\theta/\lambda$, where θ is the Bragg angle in degrees) of 2.3 to 7.8 Å $^{-1}$ and an azimuth angle (ϕ) range of 50° about the LD or TD. For (ii), only the two detectors containing diffraction rings from the LD were integrated, using a wider Q range of 2.3 to 8.6 Å⁻¹ and a narrower ϕ range of 10° about the LD. In both cases, the integration was performed over a range of ϕ , rather than over the entire cone of the diffraction space (i.e., $0 < \phi < 360$) because the gaps between the four flat panel detectors would have biased the comparison in

the heights of peaks with various Q positions. For instance, for reflections at lower Q positions, the peak encountered a lesser fraction of detector relative to the gap or bezels between the detectors, which would have the effect of reducing the measured peak intensity.

Figure 1(b) shows an integrated lineout of QP980 using the (i) integration parameters. Two crystal structures were indexed from the integrated lineouts of QP980 and QP1180: FCC ($a_\gamma \approx 3.55$ Å) and BCC ($a_\alpha \approx 2.86$ Å). The FCC peaks were created by austenite, while the BCC peaks were created by a combination of several phases/microconstituents including ferrite, martensite, and perhaps bainite, as each have similar lattice parameters and cannot be resolved in the setup utilized here. To determine the austenite volume fraction at various stages of deformation, the integrated intensities of the BCC and FCC peaks were compared after Cullity [53]. The amount of new martensite that was formed because of DIMT (f_ε^{W}) was calculated based on the austenite content before deformation ($f_{\varepsilon=0}^{W}$) and after deformation (f_ε^{W}) (Eq. (3)):

$$f_{\varepsilon}^{\alpha\prime} = f_{\varepsilon=0}^{\gamma} - f_{\varepsilon}^{\gamma} \tag{3}$$

The lineouts created using the (ii) integration parameters were used to determine the lattice strains and stresses on individual-phases relative to the loading direction. First, the lattice strains (e_{ε}^{hkl}) were calculated based on the lattice spacing (d_{ε}^{hkl}) using Eq. (4) [13,53]. The lattice spacing prior to deformation $(d_{\varepsilon=0}^{hkl})$ was determined empirically from the HEXRD data of an unloaded specimen:

$$e_{\varepsilon}^{hkl} = \frac{d_{\varepsilon}^{hkl} - d_{\varepsilon=0}^{hkl}}{d_{\varepsilon=0}^{hkl}} \tag{4}$$

Due to the HEXRD diffraction geometry and the (ii) integration parameters, the calculated lattice strains were nominally parallel to the LD, *i.e.*: e_{11}^{hkl} . Elastic stresses normal to the LD for individual planes of FCC and BCC-indexed phases, *i.e.*, $\sigma_{\gamma,11}$ and $\sigma_{\alpha,11}$, were estimated based upon Hooke's law using Eqs. (5) and (6) [13]:

$$\sigma_{\gamma,11} = E_{\gamma} e_{\gamma,11}^{311} \tag{5}$$

$$\sigma_{\alpha,11} = E_{\alpha} e_{\alpha,11}^{211} \tag{6}$$

The γ {311} and α {211} peaks were selected for analysis because they are known to exhibit strains similar to the bulk strains of BCC and FCC materials [13,54,55]. The diffraction elastic moduli of austenite and ferrite, E_{γ} and E_{α} , were assumed to be equal to 200 and 210 GPa, respectively [13].

To quantify lattice microstrain, which is known to be proportional to the total dislocation density [56], the (ii) lineouts were analyzed using X-ray diffraction line profile analysis (XRD-LPA). The basis for XRD-LPA is that lattice strain broadening is strongly {\it hkl}-dependent. Thus, the lattice microstrain or dislocation density can be assessed based on the slope of the peak breadth, ΔK_{hkl} , versus the diffraction vector, $K_{hkl} = 2 \sin\theta/\lambda$. For elastically isotropic materials, the relation of ΔK_{hkl} versus K_{hkl} is given by the Conventional Williamson Hall (CWH) equation [56,57], where D is the crystallite size, b is the magnitude of the Burgers vector and ρ is the dislocation density:

$$\Delta K_{hkl} = \frac{0.9}{D} + K_{hkl}(0.263b\sqrt{\rho}) \tag{7}$$

Prior to XRD-LPA analysis, the instrumental broadening associated with the 1-ID diffraction geometry was removed from the experimental peak breadths using Gaussian correction [58]. The peak breadth appeared to increase nonlinearly as a function of K_{hkl} . Nonlinear {\it hkl}-dependence is commonly associated with strain anisotropy [57,59–61], and it is suggested that the *Direct Fitting* Williamson-Hall (DF-WH) approach, proposed by Takaki [61],

could enhance the reliability of the strain measurements. The DF-WH method proposes that strain anisotropy can be corrected using the diffraction Young's modulus ratio (ω_{hkl}), which relates to the diffraction Young's modulus of each reflection according to Eq. (8):

$$\Delta K = \frac{0.9}{D} + \frac{\varepsilon_{DF} K_{hkl}}{\omega_{hkl}} \tag{8}$$

where ε_{DF} is the average true microstrain contained within the X-ray interaction volume. The DF-WH method determines ω_{hkl} based on iterative evaluation of Eq. (8) to determine the closest linear fit; for this study, 500 iterations were performed over the bounds proposed by Takaki et al. [61]: $0.5 < \omega_{h00} < 1.0$, where ω_{hkl} was computed from Eq. (9) [61]:

$$\frac{1}{\omega_{hkl}} = 3.83 \left(1 - \frac{1}{\omega_{h00}} \right) H^2 + \frac{1}{\omega_{h00}}$$
 (9)

The orientation parameter, H^2 , was determined by Eq. (10) [57]:

$$H^{2} = \frac{(h^{2}k^{2} + k^{2}l^{2} + l^{2}h^{2})}{(h^{2} + k^{2} + l^{2})^{2}}$$
(10)

2.4. Post-fracture characterization

To complement the bulk diffraction and mechanical testing data, spatially-resolved EBSD maps of QP980 were recorded using a JEOL JSM-7000F Field Emission Scanning Electron Microscope (FE-SEM). Quantitative analysis of the EBSD data was performed using the MTEX software package (version 5.4.0) [62]. Crystallographic texture in the BCC phases was assessed with inverse pole figures plotted relative to the loading direction (LD-IPFs). To assess local lattice rotation associated with geometrically necessary dislocations (GNDs), kernel average misorientation (KAM) analysis was performed for fifth-order neighbors with a threshold of 10 degrees. Quantitative KAM analysis was not performed on the austenite, because the austenite volume fraction was too low after deformation to achieve satisfactory grain statistics.

SEM fractographs were recorded for every material in the secondary electron imaging mode with an FEI Quanta 600 environmental scanning electron microscope (ESEM). Using low-magnification fractographs, reduction in area was measured using ImageJ [63]. For high-magnification fractographs, "watershed" image analysis was performed to determine the size distribution of ductile dimples using the ImageJ Interactive Watershed plugin [64]. Approximately 500 to 1200 dimples were measured per test condition.

3. Results

In this section, bulk tensile testing is coupled with *in-situ* HEXRD to isolate the roles of various phases in dictating phase evolution and mechanical properties over a range of temperatures. First, the bulk tensile mechanical properties of QP980, QP1180, and DP980 are discussed. Next, the HEXRD data are used to resolve the strains and stresses on individual constituent phases, leading to an improvement of the OC model. The potency of TRIP as a strengthening mechanism is linked to DIMT kinetics though the application of DF-WH lattice microstrain analysis. Finally, lattice rotation and damage due to microvoid coalescence are quantified *ex-situ* using electron microscopy.

3.1. Bulk mechanical response

True stress (σ) *versus* true strain (ε) curves for QP980, QP1180, and DP980 deformed at temperatures of 25, 100, 175, and 250 °C are plotted in Fig. 2(a–c). For QP980 and QP1180, the initial yielding behavior was not responsive to the test temperature, from the

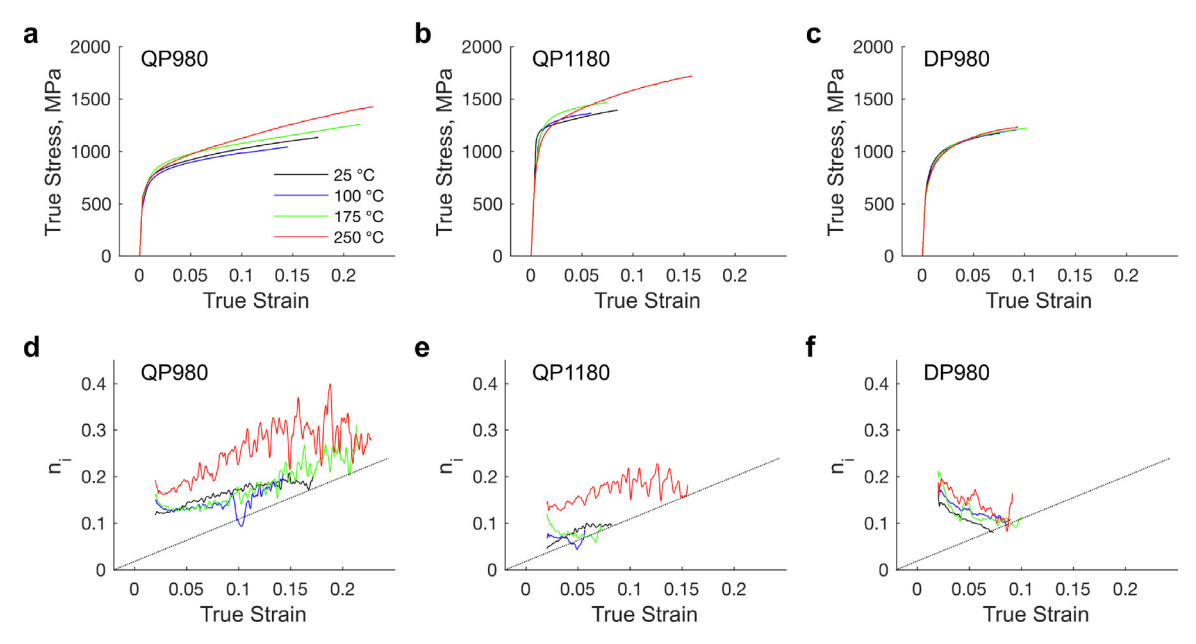


Fig. 2. Tensile-mechanical properties as a function of temperature (25, 100, 175, and 250 °C) for each steel. (a-c) True stress and (d-f) instantaneous strain hardening exponent (n_i) versus true strain curves for QP980, QP1180, and DP980, respectively. The dotted line in (d-f) represents the instability criterion, $\varepsilon = n_i$.

Table 3Tensile Mechanical Performance for Each Steel and Temperature.

Steel	Temperature	UTS	UE	$E=\int_0^{\varepsilon}\sigmad\varepsilon$
	°C	MPa	pct.	$MJ \times m^{-3}$
QP980	25	955	18.9	168
	100	904	15.6	131
	175	1015	24.0	228
	250	1136	25.8	260
QP1180	25	1281	8.9	107
	100	1288	6.1	72
	175	1364	7.8	98
	250	1471	17.0	229
DP980	25	1088	7.9	78
	100	1101	9.6	96
	175	1105	10.8	110
	250	1125	9.8	99

perspectives of yielding phenomena and the yield stress. In all cases, the transition from elastic to plastic yielding was gradual, with no clear evidence of yield point phenomena. The yield stress of each steel was qualitatively observed to be insensitive to temperature, and was on the order of 600, 710, and 1045 MPa for the QP980, DP980, and QP1180 steels, respectively. Meanwhile, the flow behavior of QP980 and QP1180 appeared to be strongly temperature dependent. In the QP980 and QP1180 steels, the specimens deformed at 250 °C exhibited the highest uniform elongation (UE) and toughness (calculated from the area under each engineering stress-strain curve, $E = \int_0^{\varepsilon_{eng}} \sigma_{eng} d\varepsilon_{eng}$), while those deformed at 100 °C exhibited the lowest toughness. The tensile behavior of the DP980 steel was similar regardless of test temperature. The tensile behavior (UTS, UE, and E) is tabulated for each steel and deformation temperature in Table 3.

To understand the temperature dependence of the ductility and toughness of QP980 and QP1180, Fig. 2(d-f) shows n_i plotted against ε . DP980 exhibited an n_i that decreased as a function of ε , which was consistent with materials that do not show the TRIP-effect. Meanwhile, QP980 and QP1180 exhibited an n_i that generally increased as a function of ε ; this behavior has been attributed to the activation of TRIP [7,8,65]. Interestingly, for the QP980 and QP1180 steels, n_i appeared to be greatly enhanced at

250 °C. The plots in Fig. 2(d-f) also show the tensile instability criterion, $\varepsilon = n_i$ [48,66]. In accordance with the instability criterion, the onset of strain localization (necking) occurred approximately when the ε versus n_i curves intersected with the $\varepsilon = n_i$ line. For this reason, the UE was maximized when n_i was relatively large at high true strains. For instance, the maximum UE and toughness was achieved for the QP980 and QP1180 at 250 °C because n_i was comparatively high, relative to the lower temperature tests.

Some serrations in the n_i curves were apparent for every steel. Similar serrations have been attributed to a combination of intermittent TRIP and dislocation slip (*e.g.*, by dynamic strain aging) [19,67,68].

3.2. Resolving martensitic transformation kinetics as a function of bulk plastic strain

It was hypothesized that the temperature-dependent strain hardening in the QP980 and QP1180 steels could be attributed to a shift in DIMT kinetics, and thus a shift in the strengthening contribution of the TRIP-effect. To investigate this phenomenon, the austenite content in the QP980 and QP1180 steels was measured with HEXRD. Figure 3(a,b) shows the austenite content as a function of true plastic strain. HEXRD revealed that each steel contained approximately 12 vol pct. austenite prior to plastic deformation $(f_{\varepsilon=0}^{\gamma})$. As the QP980 and QP1180 steels were deformed at each temperature, the austenite volume fraction as a function of true strain $(f_{\varepsilon}^{\gamma})$ decayed, while the martensite volume fraction increased. Only α '-martensite was indexed in the diffraction patterns; no ε -martensite peaks could be indexed for QP980 or QP1180, regardless of the deformation temperature, suggesting that ε -martensite did not measurably accumulate during deformation. The kinetics of DIMT appeared to be connected to the deformation temperature. For instance, DIMT appeared to be minimized at 100 °C and maximized at 250 °C.

To quantitatively assess the temperature dependence of DIMT, the HEXRD data were fit to the OC and BM models using *bulk plastic strain* as the independent variable. Both fitting approaches appeared to fit well for the QP980 and QP1180 steels at lower test temperatures, but not at higher temperatures. Because a poor fit was achieved for both models at elevated temperatures, the BM

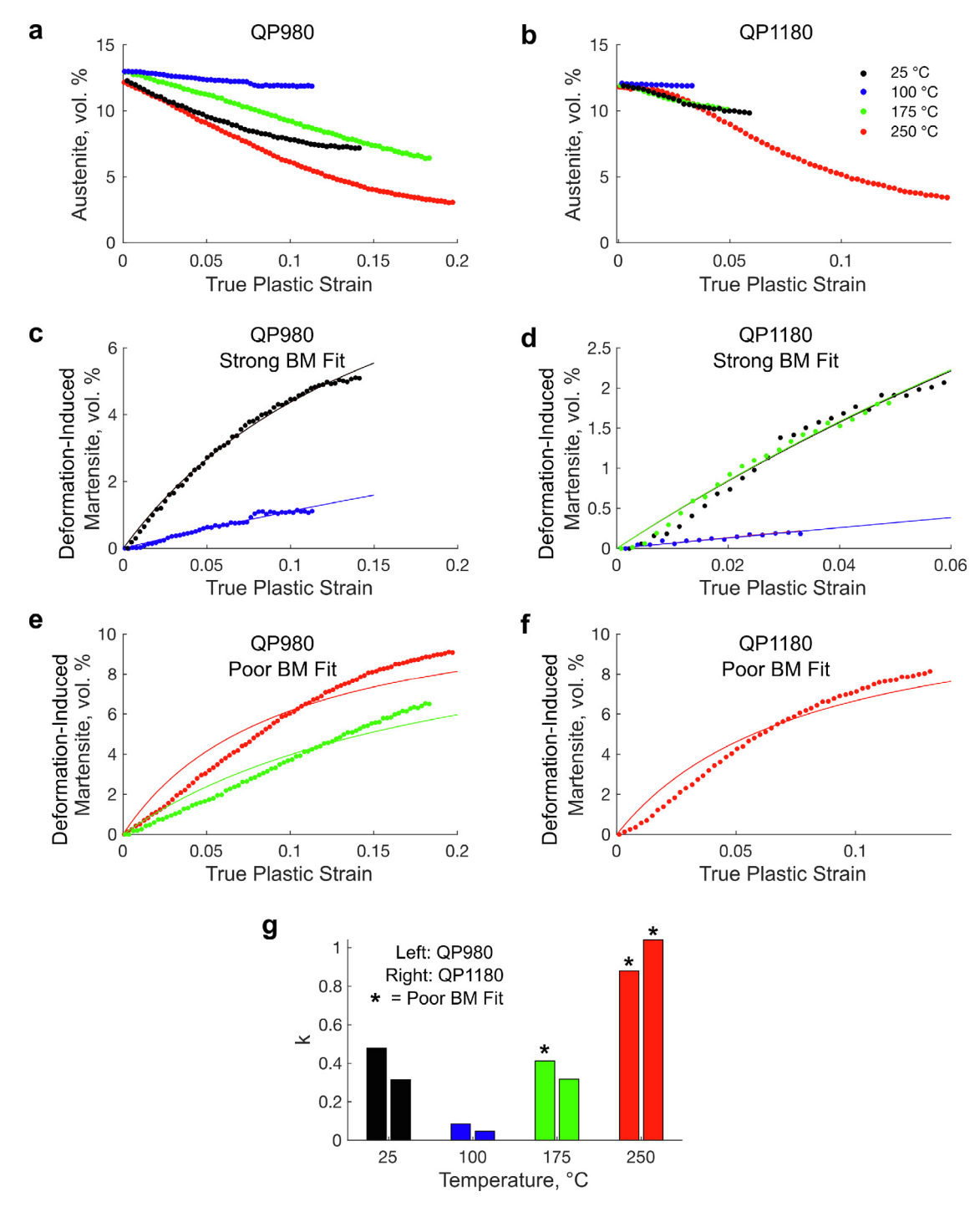


Fig. 3. Austenite content as a function of true *plastic* strain for (a) QP980 and (b) QP1180. Burke-Matsumura (BM) model fits for (c and e) QP980 and (d and f) QP1180 separated by fit quality. A summary of the austenite stability parameter (*k*) determined from the BM model fitting is shown in (g). For all fits, an autocatalytic parameter (*p*) of one was selected, based on Samek et al. [14].

model fits are illustrated in Fig. 3(c–g), to lessen the possibility of "overfitting" the experimental data with an excessive number of iterated variables (that is, two variables for BM: p and k; three variables for OC: α , β , and n). The quality of the fits was assessed based on the maximum deviation between the model and the experimental data at a given tensile strain; a fit exhibiting a deviation greater than approximately 0.5 vol. pct. was considered poor. Interestingly, for another Q&P steel, Poling also encountered poor fit quality at elevated temperatures while using bulk strain in the OC model [69].

Upon primary iterations of the BM model fitting process, the fitting converged around p=1. This result corroborated the work of Samek et al., who argued that the auto-catalytic propagation of strain induced martensite in multiphase TRIP-assisted steels is negligible (p=1) [14]. Accordingly, during the subsequent iterations of the fitting process, p was fixed at a value of one, which led to the solutions of k shown in Fig. 3(g). For the QP980 and QP1180 steels, the variation of k as a function of temperature suggested that the maximum stability of austenite occurred at a deformation temperature of 100 °C. In

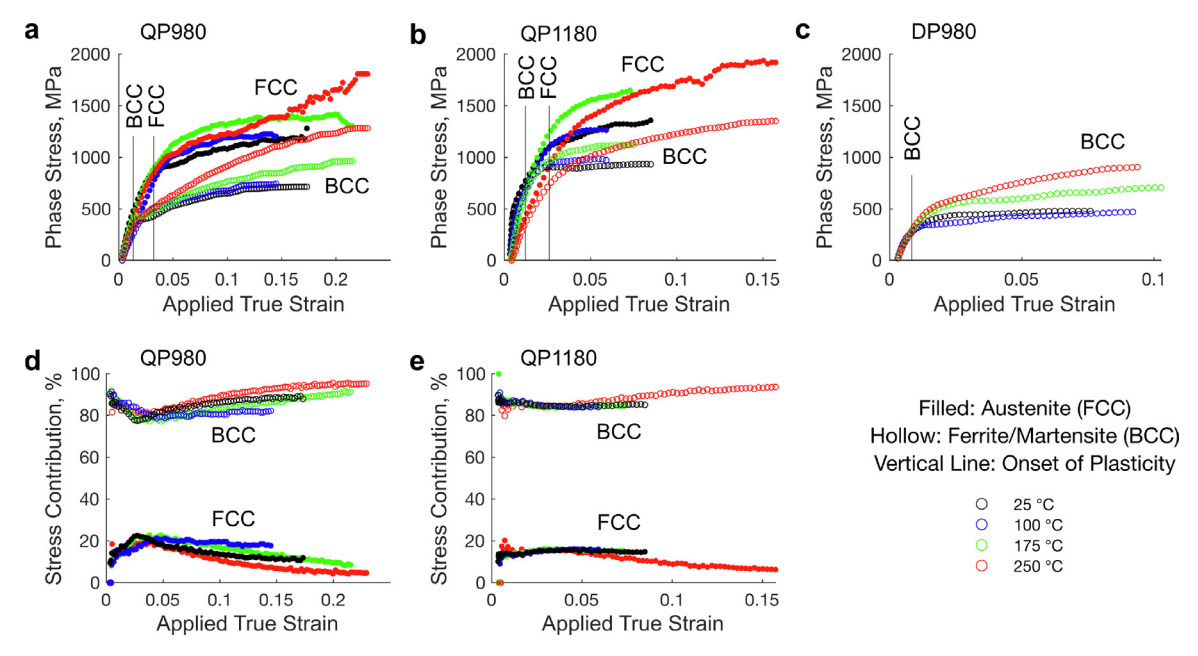


Fig. 4. Individual-phase stresses for (a) QP980, (b) QP1180, and (c) DP980. The approximate yield points for each phase at 25 °C are labeled with vertical lines. The relative stress contribution of each phase was calculated for (d) QP980 and (e) QP1180 after Harjo et al. [13].

other words, the kinetics of DIMT reached a local minimum at 100 $^{\circ}\text{C}.$

Because of the relatively long times associated with the *in-situ* HEXRD tests, the variation of k with temperature could be related to other austenite decomposition mechanisms, such as thermal decomposition to bainite [70], being active alongside of DIMT. To rule out the possibility of isothermal austenite decomposition as a mechanism for reducing the austenite content, particularly at the highest test temperature, the austenite content was measured over time in a QP980 specimen that was not deformed but simply held at 250 °C. The investigation indicated that austenite decomposition was minimal after 30 min at 250 °C in the as-received QP980; see Appendix A for details. However, the extent of isothermal decomposition in *plastically-deformed* austenite was not investigated.

3.3. Individual-phase stresses and stress partitioning in the context of the martensitic transformation

The observation that the stability of austenite in Q&P steels, and thus the toughness, is coupled to temperature with a trough-like response is not novel; for instance, Coryell et al. first revealed a similar trend for a different "QP980" steel [24]. However, to our knowledge, a robust mechanism to explain this behavior has not been confirmed in the literature [19]. Previously, stress partitioning between phases has been identified as a mechanism by which DIMT kinetics can be controlled, particularly by tuning the hardness of ferrite and martensite [71]. Thus, it was prudent assess the individual stresses in the BCC and FCC phases as a function of temperature. This section aims to elucidate stress and strain partitioning using the HEXRD data, with the eventual goal of incorporating the partitioned strain in austenite into the strain-based OC model.

Shifts in the lattice parameter, determined by HEXRD, were used to determine the stresses on individual-phases along the LD during deformation. Figure 4(a-c) shows the stresses on each phase in the three steels. For every temperature, the BCC phases yielded at a lower bulk true strain and phase stress than the austenite. Furthermore, after the onset of plasticity in each phase, the individual stresses in the austenite were higher than in the BCC phases. This observation suggested that the austenite bore an outsized share of the bulk tensile stress. For both phases in ev-

ery steel, increasing the temperature appeared to increase the apparent phase stress. This apparent increase occurred because the diffraction elastic moduli of austenite (E_{ν}) and ferrite/martensite (E_{α}) were assumed to be constant as a function of temperature for the Hooke's law calculation of the phase stresses. However, both moduli presumably decreased by nearly identical degrees as a function of increasing temperature, leading to overpredictions of the phase stress at above-ambient temperatures. Because the diffraction elastic modulus is difficult to measure experimentally, the weighted-average stress contribution technique after Hario et al. [13] was used to calculate the normalized fraction of the stress borne by each phase. In this approach, the contributed stresses, σ_c^{cont} , for each phase were individually calculated based on the phase volume fraction and the phase stresses (for example, $\sigma_{\nu}^{cont} = f_{\nu} \sigma_{\nu}^{HEXRD}$). Then, the ratio of the contributed stresses for each phase relative to the sum of the contributed stresses for both phases, $\sigma_{\nu}^{cont}/(\sigma_{\nu}^{cont}+\sigma_{\alpha}^{cont})$, was plotted in Fig. 4(d,e). The relative stress contribution of each phase was related to the DIMT kinetics for each steel and deformation temperature. As the austenite content decreased after yielding, the stress contribution from austenite decreased. For instance, for the QP980 steel deformed at 250 °C, where the DIMT kinetics were rapid, the stress contribution from austenite decreased from 15 pct. during the onset of plastic yielding to 5 pct. at the UTS. This decrease suggested that as the DIMT progressed, the bulk mechanical properties in the steels were increasingly controlled by the properties of the BCC phases.

To elucidate the progression of stress partitioning as a function of ferrite content, the ratio of stresses in the austenite *versus* the BCC phases $(\sigma_{FCC}/\sigma_{BCC})$ was plotted for the QP980 and QP1180 steels in Fig. 5. For all test conditions, once the sample deformed plastically, the ratio exceeded one, suggesting that stress was preferentially partitioned to the austenite. In general, the extent of stress partitioning to the austenite was higher in QP980 relative to QP1180. This difference was attributed to the presence of approximately 20 vol. pct. relatively soft intercritical ferrite in QP980, which likely held a disproportionately low fraction of the bulk stress. In QP980, the ratio tended to decrease as ε increased. Meanwhile, QP1180 showed a different behavior, with a ratio that tended to increase as ε increased. The root cause of this behavior was possibly due to changes in the work hardening

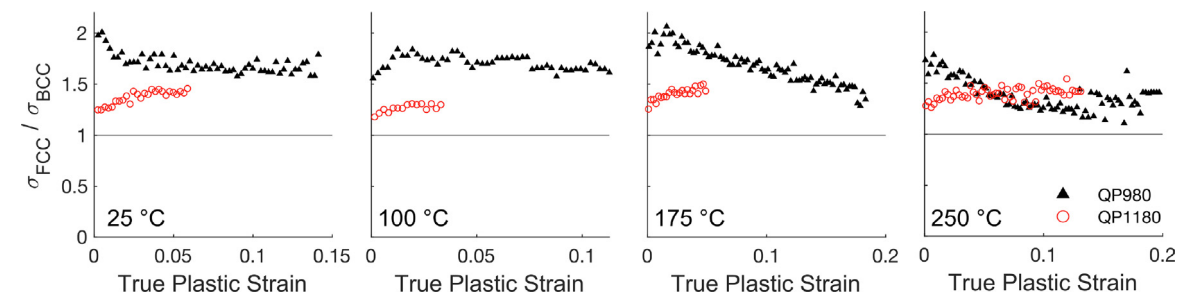


Fig. 5. Ratio of stresses in the austenite to the BCC phases $(\sigma_{FCC}/\sigma_{BCC})$ for each deformation temperature. A horizontal line is plotted at a ratio of one. Ratios above one suggest preferential stress partitioning to the austenite, and likewise, ratios below one suggest stress partitioning to the BCC phases.

Table 4 Olson-Cohen (OC) Fitting Parameters (n = 2) for QP980 and QP1180.

Steel	Temperature (°C)	α	β	R^2
QP980	25	34.8	1.3	1.00
	100	8.2	1.2	0.98
	175	7.3	2.5	0.87
	250	17.9	1.6	0.99
QP1180	25	5.1	2.5	0.97
	100	1.6	2.5	0.75
	175	3.1	1.3	0.98
	250	5.5	1.7	0.99

of the constituent phases, which are discussed in greater detail in Section 3.4.

It was hypothesized that since stress was preferentially partitioned to austenite for each steel and test temperature, strain within the austenite could diverge from the bulk tensile strain. To test this hypothesis, it was prudent to estimate the phase-specific strains in austenite. Individual constituent properties, determined by nanoindentation after Cheng et al. [10], were used to estimate the strain in the austenite. Figure 6(a) describes the process; first, the austenite stresses measured with HEXRD were compared to a $\varepsilon-\sigma$ curve generated by nanoindentation of an austenite grain within a Q&P steel of a similar composition and microstructure to QP1180. Then, the strain in the austenite was estimated based on a fit of the Hollomon equation against the stress-strain curve. The estimated strains in the austenite were plotted against the fraction of new martensite, and the curves were fit using the OC model (n = 2) for the QP980 and QP1180 steels in Fig. 6(b,c). The fitting parameters that generated the best fit for each temperature and steel are provided in Table 4.

Based on the classic interpretation of the OC model [30], the OC fit parameters measured here did not show a clear correlation between the deformation temperature and the probability of a shear band intersection forming a martensite embryo. That is, β did not appear to be strongly temperature sensitive, as it ranged from 1.2 to 2.5 for the QP980 steel and 1.3 to 2.5 for the QP1180 steel. For reference, for a steel similar to QP1180 referred to as "QP3Mn", Poling showed that β ranged from 0.7 to 1.4 over a temperature interval of 22 to 85 °C (n = 2) [22,69]. Meanwhile, α appeared to be correlated to temperature, with a similar trend progressing as a function of temperature in both steels; α was high at 25 and 250 °C, while a local minimum was reached at 100 and 175 °C. The correlation of α against deformation temperature suggested that a lack of potential martensite nucleation sites (for example, shear bands) was responsible for the diminished DIMT kinetics at intermediate temperatures. A similar downward trend in α from 25 to 100 °C was reported by Poling [22,69]. However, to our knowledge, an increase in α at higher temperatures has not been reported within the literature. Further analysis of the martensite nu-

Table 5Constants from the Linear Regression Analysis of DIMT *versus* Bulk Stress.

Steel	Temperature (°C)	K	σ_0	R^2
QP980	25	47	830	0.99
	100	134	865	0.96
	175	45	959	0.99
	250	55	872	0.99
QP1180	25	53	1263	0.98
	100	322	1290	0.90
	175	52	1350	0.99
	250	49	1289	0.99

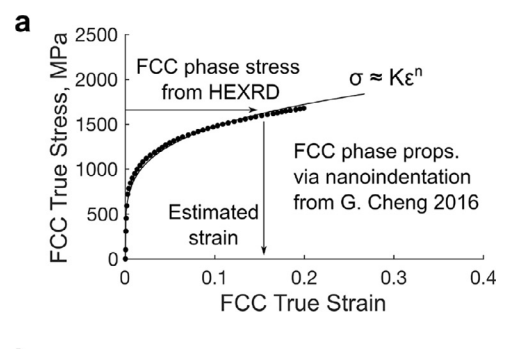
cleation site density within the austenite phase using microscopy could help to clarify the trend in α that was reported here.

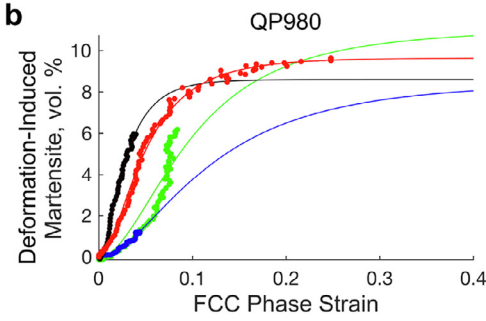
Although QP980 and QP1180 exhibited qualitatively similar trends in α as a function of temperature, QP980 exhibited an overall higher α parameter. This difference may have been due to a different austenite composition for each steel. For instance, a higher *local* manganese content of the austenite in QP980, caused by manganese partitioning during intercritical annealing, could have led to a lower stacking fault energy, a higher rate of shear band intersections, and thus a higher α parameter [30].

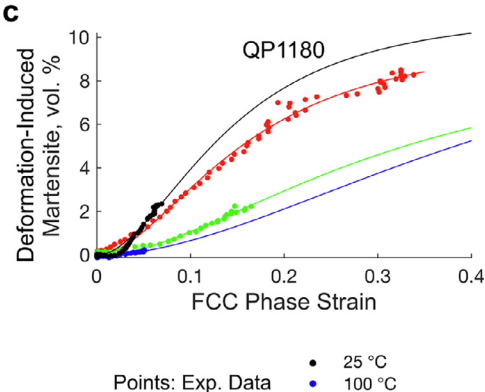
Using the austenite phase strain, rather than the bulk tensile strain, enhanced the fit quality of the OC model at elevated temperatures (175 and 250 °C). The improved fit was caused by the evolving stress partitioning to austenite as a function of strain and temperature, which led the bulk strain to poorly represent the actual strain in the austenite phase. Despite the success of the model using the austenite phase strain, the OC model was still not a perfect representation of the DIMT behavior. For example, the fits for the QP980 steel at 175 °C and QP1180 at 100 °C exhibited relatively low R^2 values of 0.87 and 0.75. Systematic errors in the experimental method could exist; for instance, it was assumed that neither the austenite constituent phase properties nor the elastic moduli changed as a function of temperature. Follow on investigations to collect higher resolution constituent phase properties as a function of temperature would resolve those inaccuracies.

3.4. Strengthening contribution of TRIP

Given that the DIMT kinetics were characterized with exceptional resolution, it was prudent to correlate DIMT with the strain hardening behavior of each steel (Fig. 7). After the onset of plastic deformation, the progression of DIMT was correlated to a linear increase in the bulk true stress, $\sigma = \sigma_0 + K f^{\alpha\prime}$. Linear regression analysis was performed to evaluate the constant terms in this expression (σ_0 and K), and the results are summarize in Table 5. The stress at which the deformation-induced martensite began to form (σ_0) appeared to be responsive to both microstructure and temperature, with the maximum σ_0 observed in the QP980 and QP1180 steel occurring at 175 °C. Meanwhile, the proportional con-







Points: Exp. Data 100 °C Lines: OC Fits 175 °C 250 °C

Fig. 6. Individual-phase properties of austenite grains in a Q&P steel after Cheng et al. [10] were implemented to estimate the FCC phase strain based on the phase stresses measured *via* high-energy X-ray diffraction (HEXRD). A schematic of the estimation process is shown in (a). Olson-Cohen (OC) model fits for the FCC phase strain *versus* the deformation-induced martensite content for (b) QP980 and (c) QP1180.

stant (K) reached a maximum for both steels at 100 °C, and was relatively constant at 25, 175, and 250 °C. K was remarkably consistent between the steels at 25, 175, and 250 °C, suggesting that the the TRIP effect strengthened each steel to a similar extent as a function of the volume of deformation-induced martensite that formed. During the final stages of deformation before the onset of necking, the stress appeared to deviate slightly upward from the linear relation, which indicated that the potency of the TRIP-effect was enhanced at high stresses and strains.

Because the TRIP-effect strengthens materials by dislocation generation at austenite-martensite interfaces, as well as within the new deformation-induced martensite, the strengthening contribution of TRIP is directly connected to the dislocation density in the BCC phases. DF-WH analysis was performed on the HEXRD lineouts to calculate the BCC lattice microstrain, which is proportional to the dislocation density. BCC lattice microstrain is related to the bulk true plastic strain in Fig. 8(a-c). Comparing the steels prior to deformation, the BCC lattice microstrain increased as the ratio of martensite to intercritical ferrite increased. (that

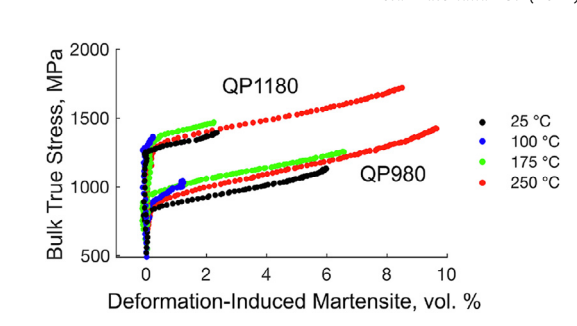


Fig. 7. Bulk true stress plotted against the amount of deformation-induced martensite, as measured *in-situ* with high-energy X-ray diffraction (HEXRD).

is, DP980<QP980<QP1180). This relationship was sensible because martensite has a higher dislocation density than proeutectoid ferrite formed during intercritical annealing. In the early stages of deformation, the presence of intercritical ferrite facilitated rapid increases in lattice microstrain as a function of tensile strain, because the soft ferrite accommodated an outsized fraction of the bulk tensile strain. For instance, the steel with the greatest fraction of intercritical ferrite (DP980) exhibited the greatest increase in lattice microstrain as a function of true plastic strain. For all steels, increasing the deformation temperature appeared to increase the BCC lattice microstrain. In the austenite-containing QP980 and QP1180, this effect was easy to rationalize because DIMT was promoted at high temperatures, leading to the formation of deformationinduced martensite with a high-dislocation density. In the DP980 which lacked an appreciable amount of austenite, the origin of the temperature sensitivity is less obvious. One explanation could be that dynamic strain aging mechanisms were increasingly active at elevated temperatures, which promoted the generation of new dislocations rather than the slip of existing dislocations, leading to an ultimately higher dislocation density and lattice microstrain. For all the steels, an additional contributing factor could be the increased activation of BCC slip systems at high temperatures. Further studies to resolve dislocation substructure and microstructure evolution as a function of temperature and strain may be useful for confirming the origin of this behavior.

Since dislocation interactions are the basis for strengthening in AHSS, it was imperative to consider the BCC phase stresses as a function of the BCC lattice microstrain. BCC phase stresses are plotted *versus* the BCC lattice microstrain in Fig. 8(d-f). The yield stress of the BCC phases for each steel and temperature are plotted as horizontal dashed lines. The BCC phase yield stresses are a combination of the yield stress in ferrite, which was presumably low, and martensite, which was presumably high. These assumptions were confirmed in the data, as the BCC yield stresses were higher in steels with a greater ratio of martensite to ferrite. Interestingly, the BCC yield stress appeared to be more sensitive to temperature in steels with a smaller ratio of martensite to ferrite. This observation seems reasonable, because relative to martensite, ferrite is strengthened extensively by short-range mechanisms, which can be overcome by thermal activation at elevated temperatures [38].

Each steel exhibited unique stress-microstrain behaviors *after yielding.* For the Q&P steels, two stages of strain hardening were observed. Meanwhile, for the DP steel, only one stage of strain hardening was observed. For discussion, the stages of strain hardening are labeled I-III in Fig. 8(d-f). In the early stages of plastic deformation in QP980 and DP980 (I), the lattice microstrain increased rapidly with minimal increases in the BCC phase stress. This rapid increase could be due to free dislocation generation and lack of dislocation interactions in intercritical ferrite, which had a long mean slip length. At the earliest stages of plastic deformation in QP1180 (II), the lattice microstrain appeared to briefly decrease with respect to the BCC phase stress. One possible expla-

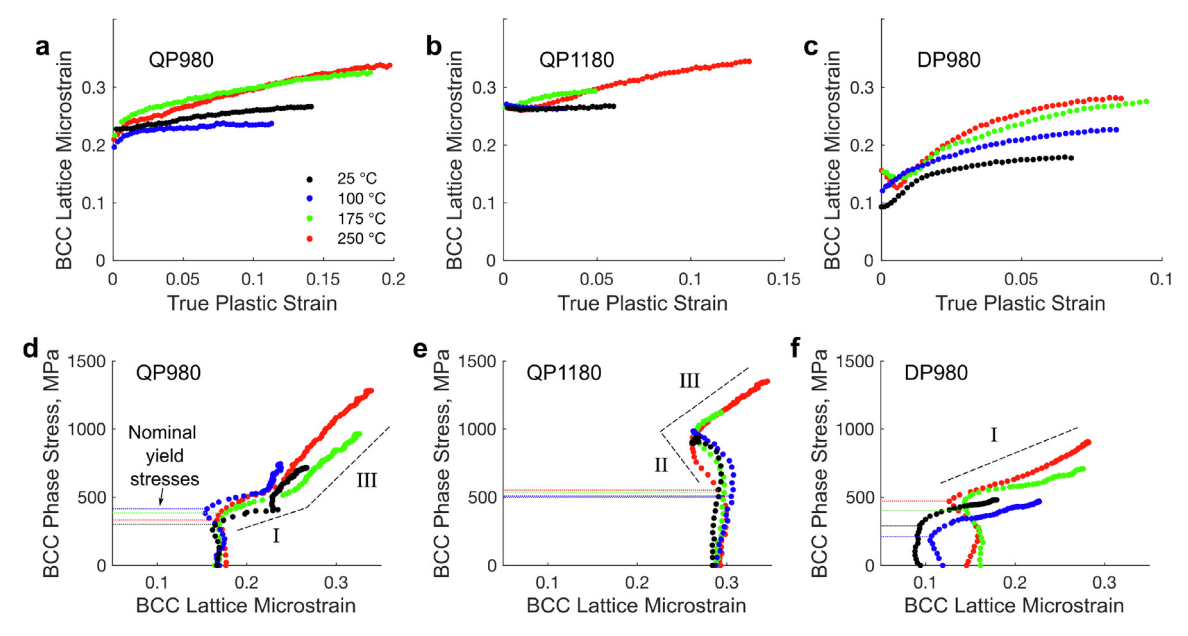


Fig. 8. BCC lattice microstrain plotted against true plastic strain (a-c) and BCC phase stress (d-f) for QP980, QP1180, and DP980. In (d-f), the nominal yield stresses of the BCC phases are labelled with horizontal lines for every test temperature. The stages of hardening in the BCC phases are labelled schematically, i.e. I-III.

nation is that the application of stresses during the mechanical loading process caused the various BCC peaks (that is, martensite and ferrite) to overlap more closely, thereby reducing the overall peak breadth and the perceived lattice microstrain. As deformation progressed, the metastable austenite-containing steels exhibited an additional strain hardening stage (III) where the BCC phase stress increased steeply as the dislocation density increased. This steep increase suggested a potent strengthening effect of the increasing fraction of new deformation-induced martensite. Interestingly, in stage III, the strengthening effect did not appear to be temperature sensitive. This is explicable because dislocation interactions contribute to strength as long-range barriers to dislocation motion, and so they have a relatively small thermal component; thus, the stress to overcome such interactions is not strongly thermally activated [38]. The use of spatially-resolved characterization techniques, such as transmission electron microscopy (TEM), are warranted to clarify the balance of dislocation generation via TRIP and/or other plasticity mechanisms (for example, Frank-Read

3.5. Microstructure and crystallographic texture evolution

To verify the trends observed *in-situ*, as well as to spatially-resolve the lattice strain and crystallographic texture evolution during deformation, EBSD maps for the QP980 steel were collected before testing and after fracture (the map was collected just outside the neck) at each temperature. In Fig. 9(a), an image quality (IQ) plus phase map reveals the substructure and morphology of each constituent phase. Two morphologically distinct types of austenite were evident. Austenite grains with an aspect ratio close to one were classified as "blocky", while grains with an aspect ratio much greater than one were classified as "film". Meanwhile, BCC grains that were devoid of significant substructure prior to deformation were classified as ferrite, while BCC grains with a prevalent substructure were classified as martensite. No deformation-induced twins were observed in the EBSD maps of QP980, regardless of the test temperature.

KAM maps, which show the magnitude of local lattice misorientation caused by the presence of geometrically necessary dislocations (GNDs), are plotted for the BCC and FCC phases in

Fig. 9(b,c). In the KAM map for the BCC phases, the ferrite appeared to exhibit a low initial KAM. Meanwhile, the martensite exhibited a higher KAM due to its high GND density. The KAM in the austenite was greater than ferrite and less than martensite. The blocky austenite appeared to exhibit a lower KAM than film austenite. The difference in KAM between blocky and film austenite was possibly due to the higher interface-to-volume ratio of the film austenite, which accumulated a higher density of GNDs during Q&P processing and during DIMT.

To quantitatively describe the lattice strain evolution, KAM histograms for the BCC phases prior to deformation and after deformation at each temperature are shown in Fig. 9(d). A bimodal distribution in the as-received condition clearly exemplified the low KAM of ferrite and the elevated KAM of martensite. After deformation at every temperature, the KAM increased, and the distributions appeared to become Gaussian, suggesting that the differences in KAM in ferrite and martensite were reduced after deformation. This evolution was consistent with the interpretation of the twostage hardening behavior of QP980 discussed previously; after the intercritical ferrite was sufficiently strain hardened such that the GND density was similar in ferrite and martensite, slip progressed simultaneously in both phases. Thus, in the uniformly-elongated sections of each specimen, the GND densities of both phases were similar. Considering temperature, the trend in the KAM generally matched the trend in BCC lattice microstrain (Fig. 8(a)). For instance, the specimens deformed at 175 and 250 °C achieved the highest uniform elongation (Fig. 2(a)), the highest BCC lattice microstrain (Fig. 8(a)), and the highest average BCC KAM (Fig. 9(d)). These results corroborated the merit of the DF-WH technique for estimating dislocation density.

To resolve longer-range lattice rotation during deformation, loading direction inverse pole figures (LD-IPF) were plotted for each EBSD scan in Fig. 9(e). Texture change was observed in the BCC phases, as $\alpha <$ 011 > directions became aligned with the LD. Meanwhile, weak texture change occurred in the austenite, as $\gamma <$ 111 > directions became aligned with the LD. The coordinated development of parallel $\alpha <$ 011 > and $\gamma <$ 111 > textures is consistent with the Kurdjumov-Sachs relationship, which has been frequently reported in TRIP-assisted steels after deformation [72–74].

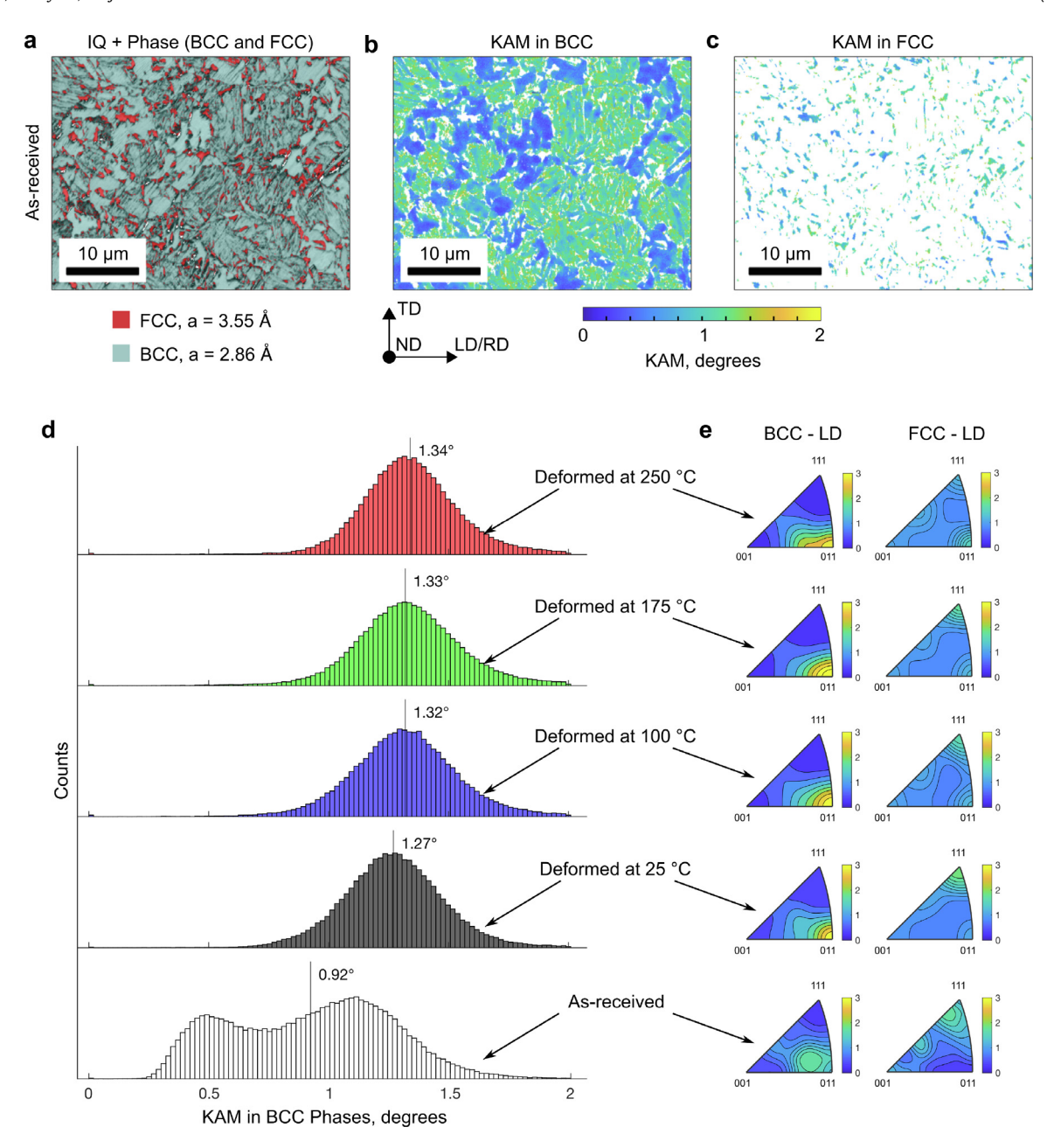


Fig. 9. Kernel average misorientation (KAM) and texture evolution was assessed using electron backscatter diffraction (EBSD) for the QP980 steel as-received and after fracture at 25, 100, 175, and 250 °C. EBSD maps were collected just outside the necked region of each fractured tensile specimen. (a) IQ + phase map of the as-received QP980, indicating the presence of ferrite, martensite, and austenite. KAM maps of (b) the BCC-indexed phases, *i.e.*, ferrite and martensite, and (c) the FCC-indexed austenite. (d) KAM distributions of the BCC-indexed phases, to compare the local lattice rotation for each specimen. The mean KAM for each distribution is plotted with a black vertical line. (e) Loading direction-inverse pole figures (LD-IPF) for the BCC and FCC-indexed phases. Units for the LD-IPFs are multiples of a random distribution.

Note that in tests with extensive DIMT (*i.e.*, QP980 deformed at 250 °C), the volume of austenite in the scan was relatively small, so there was less certainty in the FCC LD-IPFs. For instance, the FCC LD-IPF for the QP980 steel deformed at 250 °C appeared to exhibit a γ <011 > component in addition to a γ <111 > component. However, this was suspected to be due to the uncertainty of the measurement, rather than a tangible shift in texture development at 250 °C. Ultimately, the test temperature did not appreciably alter the crystallographic texture development, as each test temperature revealed a similar evolution of texture. This behavior suggested that variations in crystallographic texture evolution were not responsible for the enhanced properties of QP980 at elevated temperatures.

3.6. Fractographic analysis

SEM fractography was performed to assess local fracture ductility. In Fig. 10(a), an example SEM fractograph of a fractured specimen (QP1180 deformed at 250 °C) is shown. Evidence of diffuse necking, where the cross section at fracture was significantly smaller than that of the uniformly-elongated section, was evident on every fracture surface. The reduction of area for each tensile specimen was measured, and the results are summarized as a function of test temperature in Fig. 10(b). At low temperatures, the combination of austenite, martensite, and ferrite in QP980 achieved the highest reduction in area; this result agreed with the trends in bulk ductility shown in Fig. 2(a-c). At 250 °C, the re-

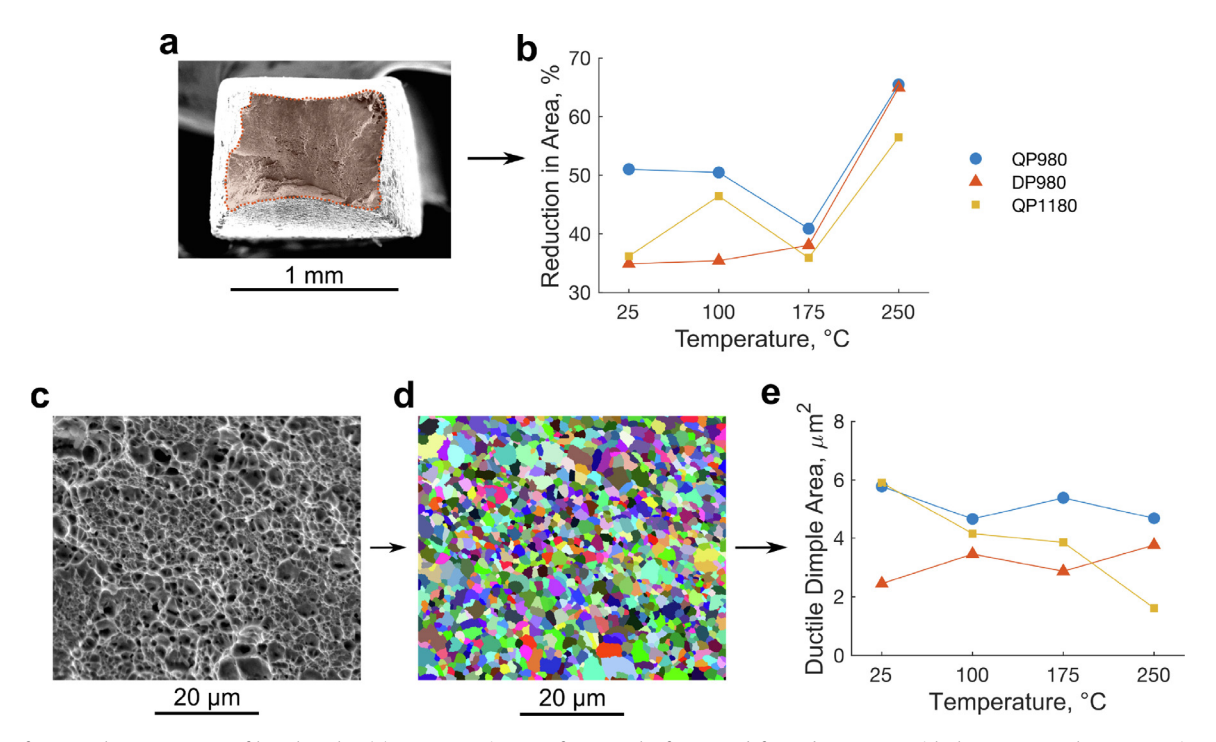


Fig. 10. SEM fractography over a range of length scales. (a) Representative SEM fractograph of QP1180 deformed at 250 °C, with the orange overlay representing the fracture surface. (b) Measurements of reduction in area for each steel and temperture. (c) Ductile dimples, commonly associated with ductile microvoid coalescence, on the surface of the same specimen. (d) Automated dimple segmentation *via* a watershed algorithm was used to collect (e) average dimple area for each steel and temperature.

duction in area was greatly enhanced for each steel relative to the lower test temperatures. It was interesting that each steel achieved similar reductions in area despite their vastly different uniform elongations. However, the direct comparison of reduction in area between the steels was not without complication, because the asreceived thickness of the DP980 steel was greater than that of the QP980 and QP1180 steels. This difference could have led to the development of different stress states in the neck, and thus different apparent fracture ductility.

To assess damage at the mesoscale, higher magnification images of the fracture surface were acquired (Fig. 10(c)). Dimples covered the entirety of every specimen, which was indicative that final fracture occurred by ductile microvoid coalescence. A watershed algorithm (Fig. 10(d)) was implemented to measure the areas of hundreds of dimples on every fracture surface. The average dimple area did not appear to significantly change as a function of test temperature. However, the average dimple area appeared to be slightly influenced by the scale of microstructure features; for instance, the highly refined DP980 exhibited the smallest average dimple area for most temperatures. Meanwhile, the QP980 exhibited the largest initial ferrite grain size and the largest average dimple area. These observations suggest that for high-strength steel microstructures, damage evolution via ductile microvoid coalescence is controlled by the scale of microstructure features and interfaces [31], and not necessarily by extrinsic deformation conditions (for example, strain rate or temperature).

4. Discussion

4.1. Measuring constituent phase properties in AHSS using HEXRD

It has been shown that the bulk properties of AHSS are fundamentally coupled with the properties of their individual constituent phases [10,72,75–77]. For instance, Du et al. showed that the bulk toughness and micromechanical deformation capacity a Q&P steel could be enhanced by tuning the plastic compatibility of tempered martensite and austenite [76]. In many studies, con-

stituent properties are determined with micromechanical testing techniques, such as micropillar compression or nanoindentation, then the constituent properties are used to interpret and predict the bulk properties [78]. There are some constraints on the practicality of using micromechanical testing to inform microstructure design. First, micromechanical testing is laborious, and so most studies only measure the properties of a handful of grains. Thus, it is difficult to capture the effects of stochastically derivative characteristics of the microstructure, like crystallographic texture, grain morphology, and local chemistry. Second, it is difficult to capture the plastic compatibility and interactions between the phases, so the choice of composite model (*i.e.*, iso-stress *versus* iso-strain) can strongly affect the predicted bulk properties [75].

With bulk mechanical testing coupled with in-situ diffraction, the behavior of the bulk is measured, with the added advantages that it is possible to resolve phase volume fraction and individualphase properties for a vast number of grains. For example, for several Q&P steels, Harjo et al. implemented neutron diffraction with bulk mechanical testing to show that tempered martensite contributed an outsized fraction of the bulk stress, while ferrite contributed relatively little [13]. Meanwhile, Hu et al. showed that in a QP980 steel, austenite was harder than ferrite, but less hard than tempered and new martensite [77]. The data collected in the present work contained less resolution of the stresses in the BCC phases, which was due to a slightly different test configuration. In this experiment, the 2θ range was maximized to capture a larger number of FCC and BCC peaks for phase volume fraction and Williamson Hall analysis. By increasing the 2θ range, the 2θ resolution was decreased, which made it difficult to deconvolve the overlapping peaks of ferrite and martensite formed during the Q&P process, and new martensite formed during deformation. Thus, all BCC-indexed phases were treated as a single phase, so the aggregate data did not represent either martensite or ferrite, but a combination of both. Here, it was observed that the BCC phases yielded prior to the austenite in both Q&P steels at each temperature. Furthermore, the measured stresses on the austenite were higher than on the BCC phases. Despite the lack of resolution over

individual constituent properties relative to Harjo et al. [13] and Hu et al. [77], the wider 2θ range was valuable for this work because it enhanced the reliability of the phase volume fraction and DF-WH techniques, which were instrumental for interpreting the microstructure-property relationships in each steel.

The HEXRD experiment performed here elucidated critical details about constituent properties that would have been impossible to obtain with conventional ex-situ experiments. However, the data were limited in several ways. First, the lack of known diffraction elastic moduli for each phase and temperature necessitated the use of approximated values from the literature ($E_{\gamma} = 200$ GPa and $E_{\alpha} = 210$ GPa) [13]. This assumption likely led to an overprediction of the phase stresses at elevated temperatures, because the elastic modulus is known to decrease with increasing temperature. Fortunately, the use of the stress contribution and stress ratio alleviated the need for accurate absolute stress measurements, as the stresses of each phase were comparatively assessed with respect to each other, and the temperature effects were assumed to be equivalent for a given condition. The second limitation was that residual stresses, existing prior to mechanical testing, were not resolved. All stresses were measured assuming that the 2θ position of each peak prior to tensile deformation represented a stress of zero. However, some residual stresses likely existed in the steels because of Q&P processing, e.g., due to the volume expansion linked with the martensitic phase transformation on cooling. A third limitation of the test configuration was that bulk texture could not be resolved, because the HEXRD data represented only one slice of reciprocal space relative to the LD axis. If the samples were rotated around the LD during deformation, then bulk texture could have been resolved in-situ. This modification would have been interesting because the crystallographic texture of each constituent likely plays a role in dictating slip activation (i.e., by Schmid's law [48]), dislocation interactions, and DIMT. Full-field bulk texture measurements will be extraordinarily important for further developing our understanding of plasticity in Q&P steels. This type of measurement is particularly important because Q&P steels exhibit low austenite fractions and small austenite grains, which makes EBSD-based crystallographic texture measurements challenging.

4.2. Operative plasticity mechanisms and DIMT model selection

At temperatures below the M_s^{σ} , the stress-assisted martensitic transformation in multiphase steels is known to be accompanied by yield point phenomena and a pronounced temperature dependence of the yield stress [79,80]. Meanwhile, at temperatures above the M_s^{σ} , initial yielding of austenite occurs by continuous dislocation slip in austenite, which has the effect of suppressing yield point phenomena [79,80]. The occurrence of roundhouse yielding and the lack of a change in the yield stress at all test temperatures suggested that the M_s^{σ} temperature was lower than 25 °C for both steels. To further evaluate the austenite stability, $M_{\rm S}$ was estimated for QP980 and QP1180 using Andrews's empirical relation [81], based on the carbon content of austenite measured with HEXRD (Appendix A) as well as the assumption of complete manganese partitioning to austenite during intercritical annealing in QP980. M_s was determined to be -45 and -21 °C for QP980 and QP1180, respectively. The mechanical evaluation of yielding behavior and the quantitative estimation of M_s confirmed that DIMT was strain-assisted for the steels and temperatures investigated here. This observation was consistent with the design intent of modern Q&P steels, and justified the use of strain-based kinetics models for interpreting the DIMT behavior.

Ruling out the accumulation of a significant fraction of deformation-induced ε -martensite was also of interest, because stacking fault energy is known to increase with increasing defor-

mation temperature. Based on the HEXRD data, no detectable fraction of ε -martensite was discovered, suggesting that plasticity was accommodated only by the $\gamma \to \alpha$ ' martensitic transformation and by dislocation generation and motion.

4.3. Effect of stress partitioning on DIMT kinetics

The HEXRD data became exceedingly useful when they were coupled with constituent stress-strain relationships determined with micromechanical testing (Fig. 6). By estimating the strain in austenite using a combination of HEXRD and nanoindentation data [10], the goodness of fit of the OC model was greatly improved relative to the same model calculated with the bulk tensile strain. This improvement suggested that stress partitioning plays a decisive role in determining the kinetics of DIMT. For instance, for the QP980 steel deformed at 175 and 250 $^{\circ}\text{C}$, a strong deviation in the stress ratio $(\sigma_{FCC}/\sigma_{BCC})$ was observed as a function of bulk tensile strain, suggesting that the extent of the stress partitioning changed as the samples deformed (Fig. 5). Likewise, the bulk tensile strain provided a poor fit against both the BM and OC models (Fig. 3), while the estimated strain in austenite provided a better fit (Fig. 6). It is theorized that constituent phase strain data measured with HEXRD would be useful for other multiphase materials that use martensitic phase transformations for strengthening. This result demonstrates the growing utility of bulk mechanical testing coupled with in-situ diffraction analysis.

Constituent properties measured with HEXRD elucidated the influence of the ratio of martensite to ferrite on strain partitioning and DIMT kinetics. The QP980 steel, which exhibited a smaller ratio of martensite to ferrite, underwent greater partitioning of stress to austenite (Fig. 5). This stress partitioning resulted in more rapid DIMT kinetics relative to the bulk tensile strain in QP980 when compared to QP1180 (Fig. 3). The causal relationship between stress partitioning and DIMT kinetics would have been impossible to measure *ex-situ*, because the elastic phase strains and stresses would have been recovered upon unloading.

4.4. Influence of dynamic strain aging

It was shown that the changes in the stress ratio ($\sigma_{FCC}/\sigma_{BCC}$) as a function of strain and temperature appeared to impede the ability of the strain-based kinetics models to correctly represent the kinetics of DIMT. For QP980, it is suspected that the decreasing stress ratio at elevated temperatures was due to activation of dynamic strain aging in the BCC phases, which had the effect of increasing the stresses in the BCC phases relative to the austenite.

The primary evidence for the activation of dynamic strain aging at elevated temperatures is that the amplitude of serrations in the instantaneous strain hardening exponent (n_i) appeared to increase in frequency and amplitude at higher temperatures for both QP980 and QP1180 (Fig. 2). Due to the nature of the n_i -term, which was computed based on a derivative of data containing some intrinsic noise (i.e., from the load cell), some serrations in n_i were expected, even in the absence of dynamic strain aging. Thus, it was prudent to confirm the presence of serrations in the true stress-strain data. Figure 11 shows true stress-strain curves for QP980, plotted over a range of true strains from 0.12 to 0.14. The data show the presence of serrations existing with greater amplitude and frequency at increasing temperatures. For instance, serrations were not obvious at 25 °C. Meanwhile, mild serrations were observed at 100 °C, and appeared to increase in quantity and amplitude at 175 and 250 °C.

The presence of serrations suggested that dynamic strain aging was increasingly active at elevated temperatures. This agreed with recent work by Mola et al., who observed the activation of serrated flow with increases in the deformation temperature over a range of 25 to 200 °C for a metastable austenitic steel [82].

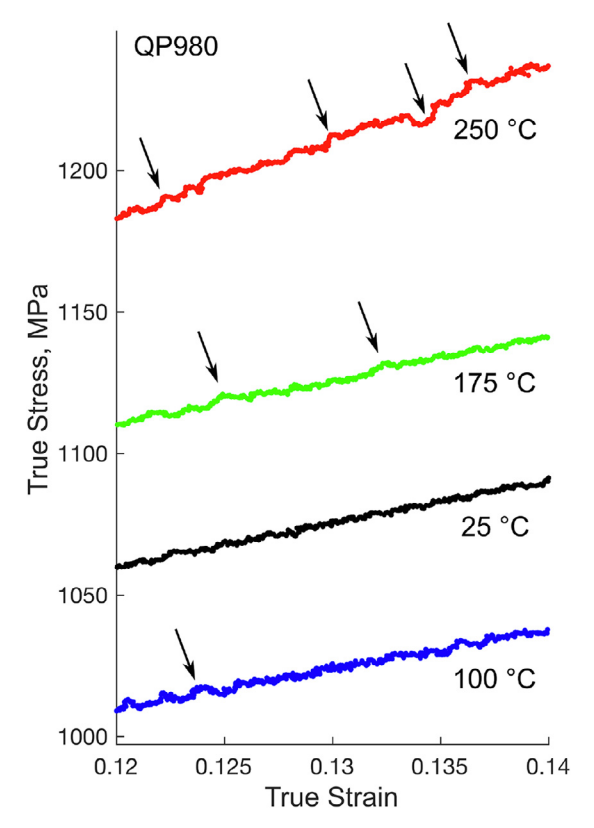


Fig. 11. True stress-strain curves of QP980 at each temperature, plotted over a narrow strain range to show the increasing magnitude and number of serrations (marked with arrows) as a function of temperature.

Mola et al. proposed that dynamic strain aging in steels containing metastable austenite over the temperature range of 25 to 200 °C is caused by dislocation pinning at martensite/austenite boundaries, and accelerated carbon diffusion out of deformation-induced martensite to those boundaries [82]. It is noted that the carbon content in austenite was determined by HEXRD to be 1.16 wt percent (see Appendix A). Thus, the deformation-induced martensite nominally contained 1.16 wt percent carbon, while the carbon content of martensite predicted by the constrained carbon equilibrium model after Speer et al. is near zero [83,84]. Thus, the argument by Mola et al. is sensible, because there was a clear driving force for carbon diffusion from the deformation-induced martensite to austenite, and carbon diffusion times in martensite are known to be comparatively short for the temperatures of interest here [82]. Since dynamic strain aging may have been important for controlling the stress contribution of the BCC phases, it is important to note that the mechanical properties and martensitic transformation kinetics reported here could be responsive to the imposed strain rate. This is because dynamic strain aging may only be activated when dislocation velocities are sufficiently slow to allow coincident carbon diffusion. In future work, it will be important to investigate the strain rate sensitivity of the phenomena reported here. However, performing HEXRD-based experiments at dynamic rates will introduce new challenges, such as a greatly deteriorated signal-to-noise ratio and resolution.

4.5. Competing microstructure development processes at elevated temperatures

In addition to dynamic strain aging, numerous competing microstructure development processes were likely active during the elevated-temperature quasi-static tests, which could have influenced the chemical stability of austenite and the properties of the

deformation-induced martensite. For instance, the duration of the plastic portion of the tensile test of QP980 at 250 °C was ~35 min (2100 s). Quasi-static tensile tests at elevated temperatures can be considered akin to a tempering or "one-step" partitioning treatment during deformation; for instance, Yan et al. reported significant austenite retention and carbon enrichment (~10 vol percent austenite having a carbon content of 0.88 wt percent) was reached during a one-step Q&P treatment of a 0.20C-1.58Si-1.55Mn steel after partitioning at 250 °C for 1000 s [85]. This would suggest that carbon partitioning from the deformation-induced martensite into the adjacent retained austenite could have increased the chemical stability of the remaining austenite in the elevated temperature tests of QP980 and QP1180. It is important to note that the carbon content of the austenite during mechanical loading could not be confirmed with the HEXRD data presented in this study, because the austenite lattice parameter shifted due to the imposed tensile stresses. The austenite carbon content during the static aging test of QP980 at 250 °C did not change significantly (see Appendix A), however, the in the static aging condition, no deformation-induced martensite was formed during that test because no deformation was imposed. During the same static aging test, approximately one volume percent austenite was lost from the microstructure without an applied tensile strain. This suggested that some austenite may have decomposed to bainite during the test.

The mechanical properties of the deformation-induced martensite may have dynamically changed *via* tempering during testing at 250 °C. For instance, dislocation recovery and carbide precipitation have been reported during Q&P treatments similar to the times and temperatures investigated here [86], which could have the effect of changing the work hardening characteristics of the martensite [39]. Moving forward, understanding these competing microstructure development mechanisms during elevated-temperature deformation experiments will be critical for understanding the warm forming response of TRIP-assisted steels, by clarifying the origin of the the temperature and strain-dependent stress partitioning that was reported here.

4.6. Adjusting temperature during sheet forming to tune the stability of austenite and the mechanical properties

The data presented here suggested that the deformation temperature affects the stability of austenite by a few mechanisms. First, the stress partitioning between the phases appeared to be temperature sensitive. For instance, at strains near the onset of strain localization, $\sigma_{FCC}/\sigma_{BCC}$ decreased as a function of increasing temperature for QP980 (Fig. 5). Hardening of the BCC phases relative to the austenite, perhaps by dynamic strain aging in the BCC phases, had the effect of partitioning strain to the austenite. For instance, at 250 °C, the estimated FCC phase strain at the UTS was \sim 0.25 for QP980 (Fig. 6), while the bulk plastic tensile strain was \sim 0.20 (Fig. 3(a)). This increased strain partitioning to austenite enhanced the kinetics of DIMT at high temperatures. Second, the number of martensite nucleation sites, as estimated by the OC model, appeared to exhibit a trough with respect to temperature that influenced the DIMT kinetics and the toughness of each steel (Table 4). This may have been due to a change in the stacking fault energy of austenite, leading to a change in the average stacking fault width, and thus a change in the volume of potential stacking fault intersections available to form a martensite embryo [30]. Detailed characterization of shear bands within the deformed microstructures, e.g., with interrupted mechanical tests and transmission electron microscopy, will be required to determine which of these mechanisms, or a combination of both mechanisms, governs the DIMT kinetics as a function of temperature.

These observations, coupled with previous work by the authors [36] and by others [21,24], suggest that temperature can

be used in conjunction with strain rate to tune the stability of austenite during sheet forming operations. For example, the greatest DIMT and toughness was achieved for the QP980 and QP1180 steels at 250 °C, which would suggest that warm stamping could be used to maximize the formability of both steels. Likewise, if less formability was required to create a specific shape, then forming at 100 °C could be used to retard DIMT, thereby preserving the austenite so that the TRIP-effect could enhance the toughness of the formed part in service. In each case, using deformation temperature as a lever to control austenite stability could be simpler than developing more elaborate Q&P thermal processing pathways and alloy compositions to manage chemical stability.

5. Conclusions

Austenite-containing AHSS, such as steels processed with the Q&P method, offer enhanced property combinations, due to the TRIP-effect and the controlled presence of several constituent phases (that is, martensite, ferrite, and austenite). The deformation responses of several AHSS with differing phase fractions were characterized by a combination of *bulk* HEXRD and *spatially-resolved* EBSD. This study constitutes the first concurrent measurements of stress partitioning and DIMT kinetics in Q&P steels for temperatures pertinent to industrial sheet forming processes. From this work, the following conclusions were made:

- 1. HEXRD resolved the DIMT kinetics for temperatures from 25 to 250 °C. Using constituent phase properties from the literature, along with individual-phase stresses resolved with HEXRD, we implemented a deformation-induced martensitic transformation kinetics model based on the partitioned strain in austenite, rather than the bulk tensile strain. This approach enhanced the ability of the Olson-Cohen model to capture the transformation behavior of the Q&P steels.
- 2. The HEXRD data showed that stress partitioning between the phases was dependent on the imposed strain, temperature, and microstructure of the steel. This suggested that tailoring the stress partitioning between the phases, for instance, by modifying the deformation temperature during sheet forming, could be used as a pathway to tune the bulk properties of austenite-containing AHSS. For instance, increasing die temperatures could change the flow properties of each constitutive phase, leading to a shift in stress partitioning, a more potent TRIP-effect, and thus greater formability.
- 3. The kinetics of DIMT were directly linked to the stress response of each steel (Fig. 7). For instance, DIMT was inactive at 100 °C, leading to low toughness and strength, while the reactivation of DIMT at 250 °C greatly enhanced the toughness and strength. The Olson-Cohen model suggested that the temperature dependence of DIMT was controlled by the number of available martensite nucleation sites, rather than the chemical driving force for transformation. This observation was used to explain the ductility trough that has been reported in the literature.
- 4. Strain evolution in ferrite and martensite was tracked using a combination of HEXRD line profile analysis and EBSD-KAM analysis. The strain evolution was temperature-dependent, due to strain partitioning between the phases and the promotion of DIMT at certain temperatures. Strain evolution was used to rationalize the temperature-dependent work hardening that was observed in the bulk specimens.

Declaration of Competing Interest

The authors declare that they have no known competing financial interests or personal relationships that could have appeared to influence the work reported in this paper.

CRediT authorship contribution statement

Christopher B. Finfrock: Conceptualization, Formal analysis, Investigation, Writing – original draft, Visualization. Benjamin Ellyson: Investigation. Sri Ranga Jai Likith: Data curation. Douglas Smith: Investigation. Connor J. Rietema: Investigation. Alec I. Saville: Investigation. Melissa M. Thrun: Investigation. Ana L. Araujo: Conceptualization, Validation, Resources. Erik J. Pavlina: Conceptualization, Validation, Resources. Jun Hu: Conceptualization, Validation, Resources. Jun Hu: Conceptualization, Validation, Funding acquisition, Project administration, Supervision. Kester D. Clarke: Conceptualization, Funding acquisition, Project administration, Project administration, Supervision.

Acknowledgements

The financial support of the Advanced Steel Processing and Products Research Center (ASPPRC), and the Center for Advanced Non-Ferrous Structural Alloys (CANFSA), a National Science Foundation (NSF) IUCRC (award no. 1624836) at the Colorado School of Mines, Golden, CO, is gratefully acknowledged. This research used resources of the Advanced Photon Source, a U.S. Department of Energy (DOE) Office of Science User Facility at Argonne National Laboratory and is based on research supported by the U.S. DOE Office of Science-Basic Energy Sciences, under Contract No. DE-AC02-06CH11357. Christopher Finfrock, Melissa Thrun, and Kester Clarke acknowledge support from the National Science Foundation division of Civil, Mechanical and Manufacturing Innovation (NSF-CMMI) through award no. 1752530. Benjamin Ellyson, Sri Ranga Jai Likith, and Amy Clarke were supported by the U.S. Department of the Navy, Office of Naval Research under ONR award no. N00014-18-1-2567. Any opinions, findings, and conclusions or recommendations expressed in this material are those of the author(s) and do not necessarily reflect the views of the Office of Naval Research. Connor Rietema was supported under the auspices of the U.S. Department of Energy by Lawrence Livermore National Laboratory under Contract DE-AC52-07NA27344. Alec Saville was supported by the National Science Foundation Graduate Research Fellowship, USA, under Grant no. 2019260337.

Appendix A. Evaluating the propensity for austenite decomposition and carbon partitioning during static aging at 250 $^{\circ}\text{C}$

To determine whether any austenite decomposition mechanisms were active at the highest test temperature, a QP980 specimen was held at 250 °C for 30 min without a tensile load, while HEXRD data was collected. This condition was referred to as "static aging". To compare the static aging condition against a sample deformed to failure, a plot of austenite fraction versus time for each test is given in Fig. A.1. In the "deformation to fracture" specimen, the onset of plastic deformation occurred after approximately five minutes.

In the static aging condition, the austenite content in QP980 decreased from 13 to 12 vol. pct. after 30 min at 250 °C. This decrease suggested that some austenite decomposition mechanisms were active for the times and temperatures of interest in this study. However, this amount was small, and was likely not detectable with common measurement techniques, like ex-situ EBSD or X-ray diffraction. Meanwhile, in the specimen deformed to fracture, the austenite content decreased from 13 to 3 vol. pct. Thus, by comparing the two behaviors, it was inferred that during the tensile tests, most of the austenite transformed because of DIMT (\sim 9 vol. pct.), while a small fraction transformed because of austenite decomposition (\sim 1 vol. pct.).

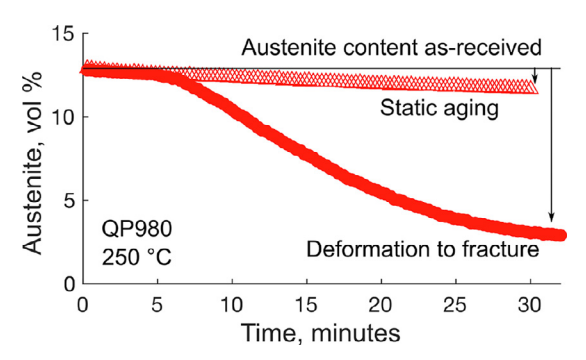


Fig. A.1. Austenite content *versus* time in minutes for two samples of QP980 held at $250\,^{\circ}$ C. The "static aging" sample was not deformed. The second sample was deformed to fracture. The onset of plastic deformation occurred after approximately five minutes.

The lattice parameter (a_0) of each austenite peak, γ {111}, γ {200}, γ {220}, γ {311}, γ {222}, and γ {331} was calculated based on the d-spacing (d_{hkl}) determined from HEXRD after Eq. (A.1):

$$a_0 = d_{hkl} \times \sqrt{h^2 + k^2 + l^2} \tag{A.1}$$

The mean lattice parameter (\bar{a}_0) was calculated based on a_0 from the six peaks. Prior to any heating, \bar{a}_0 was determined to be 3.6060 and 3.6047 Å for QP980 and QP1180, respectively. The carbon content of the austenite (C_γ) was *estimated* based on Eq. (A.2) after Cullity [53]:

$$\bar{a}_0 = 3.555 + 0.044C_{\gamma} \tag{A.2}$$

Solving Eq. (A.2) suggested that C_{γ} was equal to 1.16 and 1.13 wt percent for QP980 and QP1180. During the 30 min static aging treatment at 250 °C, \bar{a}_0 increased by 0.00072 Å for QP980. This suggested that carbon partitioning to austenite was minimal during static aging, on the order of \sim 0.016 weight percent. It is noted that because HEXRD is a bulk measurement technique, \bar{a}_0 and C_{γ} describe the average of all the austenite grains within the interaction volume of the X-ray beam. Thus, some variations in \bar{a}_0 and C_{γ} could have existed due to variations in local residual stresses and carbon content, but those variations could not be resolved without supplemental techniques (e.g., atom probe tomography).

References

- P.M. Kelly, L.R.F. Rose, The martensitic transformation in ceramics Its role in transformation toughening, Prog. Mater. Sci. 47 (5) (2002) 463–557, doi:10. 1016/S0079-6425(00)00005-0.
- [2] L. Wang, T. Cao, X. Liu, B. Wang, K. Jin, Y. Liang, L. Wang, F. Wang, Y. Ren, J. Liang, Y. Xue, A novel stress-induced martensitic transformation in a singlephase refractory high-entropy alloy, Scr. Mater. 189 (2020) 129–134, doi:10. 1016/j.scriptamat.2020.08.013.
- [3] F.G. Coury, D. Santana, Y. Guo, J. Copley, L. Otani, S. Fonseca, G. Zepon, C. Kiminami, M. Kaufman, A. Clarke, Design and in-situ characterization of a strong and ductile co-rich multicomponent alloy with transformation induced plasticity, Scr. Mater. 173 (2019) 70–74, doi:10.1016/j.scriptamat.2019.07.045.
- [4] J.A. Copley, F.G. Coury, B. Ellyson, J. Klemm-Toole, J. Frishkoff, C. Finfrock, Z. Fisher, N. Kedir, C. Kirk, W. Chen, N. Parab, T. Sun, K. Fezzaa, K.D. Clarke, A.J. Clarke, In-situ observation of FCC-HCP transformation-induced plasticity behavior during dynamic deformation of CoCrNi multi-principal element alloys, Metall. Mater. Trans. A (2022), doi:10.1007/s11661-022-06636-y.
- [5] S.W. Lee, J.M. Oh, C.H. Park, J.K. Hong, J.T. Yeom, Deformation mechanism of metastable titanium alloy showing stress-induced α-martensitic transformation, J. Alloys Compd. 782 (2019) 427–432, doi:10.1016/j.jallcom.2018.12.160.
- [6] B. Ellyson, J. Klemm-Toole, K. Clarke, R. Field, M. Kaufman, A. Clarke, Tuning the strength and ductility balance of a TRIP titanium alloy, Scr. Mater. 194 (2021) 113641, doi:10.1016/j.scriptamat.2020.113641.
- [7] W. Bleck, X. Guo, Y. Ma, The TRIP effect and its application in cold formable sheet steels, Steel Res. Int. 88 (10) (2017), doi:10.1002/srin.201700218.
- [8] C.B. Finfrock, A.J. Clarke, G.A. Thomas, K.D. Clarke, Austenite stability and strain hardening in C-Mn-Si quenching and partitioning steels, Metall. Mater. Trans. A 51 (5) (2020) 2025–2034, doi:10.1007/s11661-020-05666-8.
- [9] N.J. Wengrenovich, G.B. Olson, Optimization of a TRIP steel for adiabatic fragment protection, Mater. Today 2 (2015) S639–S642, doi:10.1016/j.matpr.2015. 07.365.

- [10] G. Cheng, K.S. Choi, X. Hu, X. Sun, Determining individual phase properties in a multi-phase Q&P steel using multi-scale indentation tests, Mater. Sci. Eng., A 652 (2016) 384–395. doi:10.1016/j.msea.2015.11.072.
- [11] F. Abu-Farha, X. Hu, X. Sun, Y. Ren, L.G. Hector, G. Thomas, T.W. Brown, In-situ local measurement of austenite mechanical stability and transformation behavior in third generation advanced high strength steels, Metallurgical & Materials Transactions A 49A (2018) 2583–2596.
- [12] Y. Zhao, M.N. Cinbiz, J.S. Park, J. Almer, D. Kaoumi, Tensile behavior and microstructural evolution of a Fe-25Ni-20Cr austenitic stainless steel (Alloy 709) from room to elevated temperatures through in-situ synchrotron X-Ray diffraction characterization and transmission electron microscopy, J. Nucl. Mater. 540 (2020) 152367, doi:10.1016/j.jnucmat.2020.152367.
- [13] S. Harjo, N. Tsuchida, J. Abe, W. Gong, Martensite phase stress and the strengthening mechanism in TRIP steel by neutron diffraction, Sci. Rep. 7 (1) (2017) 2-4. doi:10.1038/s41598-017-15252-5.
- [14] L. Samek, E. De Moor, J. Penning, B.C. De Cooman, Influence of alloying elements on the kinetics of strain-induced martensitic nucleation in low-alloy, multiphase high-strength steels, Metall. Mater. Trans. A 37 (1) (2006) 109–124, doi:10.1007/s11661-006-0157-0.
- [15] W.W. Gerberich, G. Thomas, E.R. Parker, V.F. Zackay, Metastable austenites: decomposition and strength, in: 2nd Internantional Conference on the Strength of Metals and Alloys, 1970, pp. 1–6. Asilomar, Ca
- [16] B. He, On the factors governing austenite stability: intrinsic versus extrinsic, Materials 13 (15) (2020) 1–31, doi:10.3390/ma13153440.
- [17] B.B. He, M. Wang, M.X. Huang, Resetting the austenite stability in a medium mn steel via dislocation engineering, Metall. Mater. Trans. A 50 (6) (2019) 2971–2977, doi:10.1007/s11661-019-05222-z.
- [18] D.D. Adams, Characterization of the factors influencing retained austenite transformation in Q&P steels, Brigham Young University, 2020 Ph.D. thesis.
- [19] C.B. Finfrock, M.M. Thrun, D. Bhattacharya, T. Ballard, A.J. Clarke, K.D. Clarke, Strain rate dependent ductility and strain hardening in Q&P steels, Metall. Mater. Trans. A 52A (2021) 928–942, doi:10.1007/s11661-020-06127-y.
- [20] V. Savic, L. Hector, R. Alturk, C. Enloe, High Strain Rate Tensile Behavior of 1180MPa Grade Advanced High Strength Steels, Technical Report No. 2020-01-0754, SAE Technical Papers, 2020, doi:10.4271/2020-01-0754.Abstract.
- [21] C. Enloe, V. Savic, W. Poling, L. Hector, R. Alturk, Strain Rate Effect on Martensitic Transformation in a TRIP Steel Containing Carbide-Free Bainite, Technical Report No. 2019-01-0521, SAE Technical Papers, 2019, doi:10.4271/ 2019-01-0521.
- [22] W.A. Poling, E. De Moor, J.G. Speer, K.O. Findley, Temperature effects on tensile deformation behavior of a medium manganese trip steel and a quenched and partitioned steel, Metals 11 (2) (2021), doi:10.3390/met11020375.
- [23] W. Feng, Z. Wu, L. Wang, J.G. Speer, Effect of testing temperature on retained austenite stability of cold rolled CMnSi steels treated by quenching and partitioning process, Steel Res. Int. 84 (3) (2013) 246–252, doi:10.1002/srin.201200129
- [24] J. Coryell, V. Savic, L. Hector, S. Mishra, Temperature Effects on the Deformation and Fracture of a Quenched-and-Partitioned Steel, Technical Report No. 2013-01-0610, SAE Technical Papers, 2013, doi:10.4271/2013-01-0610.
- [25] C.M. Enloe, J. Coryell, J. Wang, Retained austenite stability and impact performance of advanced high strength steel at reduced temperatures, SAE Int. J. Mater.Manuf. 10 (2) (2017), doi:10.4271/2017-01-1707.
- [26] S.S. Hecker, M.G. Stout, K.P. Staudhammer, J.L. Smith, Effects of strain state and strain rate on deformation-induced transformation in 304 stainless steel: part i. Magnetic measurements and mechanical behavior, Metall. Trans. A 13 (1982) 619–626. doi:10.1007/BF02644428.
- [27] L.E. Murr, K.P. Staudhammer, S.S. Hecker, Effects of strain state and strain rate on deformation-induced transformation in 304 stainless steel: Part II. Microstructural study, Metall. Trans. A 13 (1982) 627–635, doi:10.1007/ BEO2644428
- [28] J. Hidalgo, K.O. Findley, M.J. Santofimia, Thermal and mechanical stability of retained austenite surrounded by martensite with different degrees of tempering, Mater. Sci. Eng. A 690 (2017) 337–347, doi:10.1016/j.msea.2017.03.017.
- [29] G.B. Olson, C. Morris, A mechanism for the strain-induced nucleation of martensitic transformations, J. Less-Common Metals 28 (1) (1972) 107–118, doi:10.1016/0022-5088(72)90173-7.
- [30] G.B. Olson, M. Cohen, Kinetics of strain-induced martensitic nucleation, Metall. Trans. A 6A (1975) 791–795, doi:10.1007/BF02672301.
- [31] C. Finfrock, C.G. Becker, T. Ballard, G. Thomas, K. Clarke, A. Clarke, Tensile deformation characteristics and austenite transformation behavior of advanced high strength steels considering adiabatic heating, in: Contributed Papers from Materials Science & Technology (MS&T19), 2019, pp. 1236–1243, doi:10.7449/2019/MST_2019_1236_1243. Portland, Oregon
- [32] A. Andrade-Campos, F. Teixeira-Dias, U. Krupp, F. Barlat, E.F. Rauch, J.J. Grácio, Effect of strain rate, adiabatic heating and phase transformation phenomena on the mechanical behaviour of stainless steel, Strain 46 (3) (2010) 283–297, doi:10.1111/j.1475-1305.2008.00572.x.
- [33] A.K. Ghosh, The influence of strain hardening and strain-rate sensitivity on sheet metal forming, J. Eng. Mater. Technol. 99 (3) (1977) 264–274, doi:10.1115/13443530
- [34] R. Alturk, L.G. Hector, C. Matthew Enloe, F. Abu-Farha, T.W. Brown, Strain rate effect on tensile flow behavior and anisotropy of a medium-manganese TRIP steel, JOM 70 (6) (2018) 894–905, doi:10.1007/s11837-018-2830-3.
- [35] X. Yang, L.G. Hector, J. Wang, A combined theoretical/experimental approach for reducing ringing artifacts in low dynamic testing with servo-hydraulic load frames, Exp. Mech. 54 (5) (2014) 775–789, doi:10.1007/s11340-014-9850-x.

- [36] C.B. Finfrock, D. Bhattacharya, B.N.L. McBride, T.J. Ballard, A.J. Clarke, K.D. Clarke, Decoupling the impacts of strain rate and temperature on TRIP in a Q&P steel, JOM 74 (2) (2022) 506–512, doi:10.1007/s11837-021-05039-5.
- [37] C.B. Finfrock, Temperature and strain rate dependence of the martensitic transformation and mechanical properties in advanced high strength steels, Colorado School of Mines, Golden, CO, 2022 Ph.D. thesis.
- [38] D. Hull, D.J. Bacon, Introduction to Dislocations, 5th ed., Elsevier, Burlington, MA, 2011.
- [39] K.O. Findley, J. Hidalgo, R.M. Huizenga, M.J. Santofimia, Controlling the work hardening of martensite to increase the strength/ductility balance in quenched and partitioned steels, Mater. Des. 117 (2017) 248–256, doi:10.1016/j.matdes. 2016.12.065.
- [40] J.H. Ryu, D.I. Kim, H.S. Kim, H.K.D.H. Bhadeshia, D.W. Sun, Strain partitioning and mechanical stability of retained austenite, Scr. Mater. 63 (2010) 297–299.
- and mechanical stability of retained austenite, Scr. Mater. 63 (2010) 297–299.
 [41] L. Chen, Q. Jia, S. Hao, Y. Wang, C. Peng, X. Ma, Z. Zou, M. Jin, The effect of strain-induced martensite transformation on strain partitioning and damage evolution in a duplex stainless steel with metastable austenite, Mater. Sci. Eng., A 814 (2021), doi:10.1016/j.msea.2021.141173.
- [42] S. Wei, J. Kim, C.C. Tasan, In-situ investigation of plasticity in a Ti-Al-V-Fe $(\alpha+\beta)$ alloy: slip mechanisms, strain localization, and partitioning, Int. J. Plast. 148 (2022), doi:10.1016/j.ijplas.2021.103131.
- [43] P.J. Gibbs, B.C. De Cooman, D.W. Brown, B. Clausen, J.G. Schroth, M.J. Merwin, D.K. Matlock, Strain partitioning in ultra-fine grained medium-manganese transformation induced plasticity steel, Mater. Sci. Eng. A 609 (2014) 323–333, doi:10.1016/j.msea.2014.03.120.
- [44] J. Burke, The Kinetics of Phase Transformations in Metals, Pergamon Press Inc, Long Island City, New York, 1965.
- [45] O. Matsumura, Y. Sakuma, Y. Ishii, J. Zhao, Effect of retained austenite on formability of high strength sheet steels, ISIJ Int. 32 (10) (1992) 1110–1116, doi:10.2355/isijinternational.32.1110.
- [46] C. Liu, L. Wang, Y. Liu, Effects of strain rate on tensile deformation behavior of quenching and partitioning steel, Mater. Sci. Forum 749 (2013) 401–406. 10.4028/ www.scientific.net/MSF.749.401
- [47] P. Frint, T. Kaiser, T. Mehner, E. Bruder, M. Scholze, B. Mašek, T. Lampke, M.F.X. Wagner, Strain-rate sensitive ductility in a low-alloy carbon steel after quenching and partitioning treatment, Sci. Rep. 9 (1) (2019) 1–7, doi:10.1038/ s41598-019-53303-1.
- [48] G.E. Dieter, Mechanical Metallurgy, 3rd, McGraw-Hill, New York, NY, 1961.
- [49] S. Haas, J. Andersson, M. Fisk, J.S. Park, U. Lienert, Correlation of precipitate evolution with vickers hardness in haynes® 282® superalloy: in-situ high-energy SAXS/WAXS investigation, Mater. Sci. Eng. A 711 (2018) 250–258, doi:10.1016/j.msea.2017.11.035.
- [50] G. Zhang, K. Mo, Y. Miao, X. Liu, J. Almer, Z. Zhou, J.F. Stubbins, Load partitioning between ferrite/martensite and dispersed nanoparticles of a 9Cr ferritic/martensitic (F/M) ODS steel at high temperatures, Mater. Sci. Eng. A 637 (2015) 75–81, doi:10.1016/j.msea.2015.04.037.
- [51] J.H. Lee, J. Almer, C. Aydner, J. Bernier, K. Chapman, P. Chupas, D. Haeffner, K. Kump, P.L. Lee, U. Lienert, A. Miceli, G. Vera, Characterization and application of a GE amorphous silicon flat panel detector in a synchrotron light source, Nucl. Instrum. Methods Phys. Res. Sect. A 582 (1) (2007) 182–184, doi:10.1016/j.nima.2007.08.103.
- [52] B.H. Toby, R.B. Von Dreele, GSAS-II: the genesis of a modern open-source all purpose crystallography software package, J. Appl. Crystallogr. 46 (2) (2013) 544–549, doi:10.1107/S0021889813003531.
- [53] B.D. Cullity, Elements of X-Ray Diffraction, 1st, Addison-Wesley Publishing Company, Inc., Reading, 1956.
- [54] B. Clausen, T. Lorentzen, M.A.M. Bourke, M.R. Daymond, Lattice strain evolution during uniaxial tensile loading of stainless steel, Mater. Sci. Eng., A 259 (1) (1999) 17–24, doi:10.1016/S0921-5093(98)00878-8.
- [55] M.T. Hutchings, Neutron diffraction measurement of residual stress fields-the engineer's dream come true? Neutron News 3 (3) (1992) 14–19, doi:10.1080/ 10448639208218768.
- [56] G.K. Williamson, W.H. Hall, Discussion of the theories of line broadening, Acta Metall. (1953), doi:10.1016/0001-6160(53)90006-6.
- [57] F. HajyAkbary, J. Sietsma, A.J. Böttger, M.J. Santofimia, An improved X-ray diffraction analysis method to characterize dislocation density in lath martensitic structures, Mater. Sci. Eng., A 639 (May) (2015) 208–218, doi:10.1016/j.msea.2015.05.003.
- [58] S. Takaki, T. Masumura, F. Jiang, T. Tsuchiyama, Effect of instrumental correction on X-ray line profile analysis in cold rolled ferritic steel, ISIJ Int. 58 (6) (2018) 1181–1183.
- [59] T. Ungár, I. Dragomir, Ã. Révész, A. Borbély, The contrast factors of dislocations in cubic crystals: the dislocation model of strain anisotropy in practice, J. Appl. Crystallogr. 32 (5) (1999) 992–1002, doi:10.1107/S0021889899009334.
- [60] T. Ungár, A. Borbély, The effect of dislocation contrast on x-ray line broadening: a new approach to line profile analysis, Appl. Phys. Lett. 69 (21) (1996) 3173–3175, doi:10.1063/1.117951.
- [61] S. Takaki, F. Jiang, T. Masumura, T. Tsuchiyama, Correction of elastic anisotropy in Williamson-Hall plots by diffraction Young's modulus and direct fitting method, ISIJ Int. 58 (4) (2018) 769–775, doi:10.2355/isijinternational. ISIJINT-2017-642.

- [62] F. Bachmann, R. Hielscher, H. Schaeben, Texture analysis with MTEX- Free and open source software toolbox, Solid State Phenomena 160 (2010) 63–68. 10.4028/www.scientific.net/SSP.160.63
- [63] J. Schindelin, I. Arganda-Carreras, E. Frise, V. Kaynig, M. Longair, T. Pietzsch, S. Preibisch, C. Rueden, S. Saalfeld, B. Schmid, J.Y. Tinevez, D.J. White, V. Hartenstein, K. Eliceiri, P. Tomancak, A. Cardona, Fiji: an open-source platform for biological-image analysis, Nat. Methods 9 (7) (2012) 676–682, doi:10.1038/nmeth.2019.
- [64] B. Lombardot, Interactive watershed, 2022, https://imagej.net/plugins/ interactive-watershed.
- [65] P.J. Gibbs, Design considerations for the third generation advanced high strength steel, Colorado School of Mines, 2013 Ph.D. thesis.
- [66] A.K. Ghosh, Tensile instability and necking in materials with strain hardening and strain-rate hardening, Acta Metall. 25 (12) (1977) 1413–1424, doi:10.1016/ 0001-6160(77)90072-4.
- [67] H. Du, Y. Gong, Q. Zeng, Y. Li, N. Min, X. Jin, Interpretation of dynamic strain aging in an intercritical annealed steel by dislocation multiplication induced by martensitic transformation, Metall. Mater. Trans. A (2021) 15–20, doi:10.1007/ s11661-021-06464-6.
- [68] M. Thrun, C.B. Finfrock, A. Clarke, K. Clarke, Effects of unloading on subsequent yielding behavior in 304 stainless steel, Front. Mater. 7 (2021) 1–6, doi:10.3389/fmats.2020.615361.
- [69] W. Poling, Tensile deformation of third generation advanced high strength sheet steels under high strain rates, Colorado School of Mines, 2017 Ph.D. thesis
- [70] R.M. Wu, L. Wang, X.J. Jin, Thermal stability of austenite and properties of quenching & partitioning (Q&P) treated AHSS, Phys. Procedia 50 (2013) 8–12, doi:10.1016/j.phpro.2013.11.003.
- [71] X. Tan, D. Ponge, W. Lu, Y. Xu, X. Yang, X. Rao, D. Wu, D. Raabe, Carbon and strain partitioning in a quenched and partitioned steel containing ferrite, Acta Mater. 165 (2019) 561–576, doi:10.1016/j.actamat.2018.12.019.
- [72] E.J. Seo, L. Cho, Y. Estrin, B.C. De Cooman, Microstructure-mechanical properties relationships for quenching and partitioning (Q&P) processed steel, Acta Mater. 113 (2016) 124–139, doi:10.1016/j.actamat.2016.04.048.
- [73] M. Wang, M.X. Huang, Abnormal TRIP effect on the work hardening behavior of a quenching and partitioning steel at high strain rate, Acta Mater. 188 (2020) 551–559, doi:10.1016/j.actamat.2020.02.035.
- [74] P. Barriobero-Vila, R. Jerez-Mesa, A. Guitar, O. Gavalda-Diaz, J.A. Travieso-Rodríguez, A. Stark, N. Schell, J. Llumà, G. Fargas, A. Mateo, J.J. Roa, Deformation kinetics of a TRIP steel determined by in situ high-energy synchrotron X-ray diffraction, Materialia 20 (October) (2021) 101251, doi:10.1016/j.mtla.2021. 101251.
- [75] G. Cheng, K.S. Choi, X.H. Hu, X. Sun, Computational material design for Q&P steels with plastic instability theory, Mater. Des. 132 (2017) 526–538, doi:10. 1016/j.matdes.2017.07.029.
- [76] H. Du, Y. Gong, T. Liang, Y. Li, Y. Xu, X. Lu, Q. Zeng, X. Jin, Enhancement of impact toughness via tailoring deformation compatibility of constituent phases in duplex Q&P steel with excellent strength and ductility, Metall. Mater. Trans. A 51 (5) (2020) 2097–2117, doi:10.1007/s11661-020-05701-8.
- [77] X.H. Hu, X. Sun, L.G. Hector, Y. Ren, Individual phase constitutive properties of a TRIP-assisted QP980 steel from a combined synchrotron X-ray diffraction and crystal plasticity approach, Acta Mater. 132 (2017) 230–244, doi:10.1016/j. actamat.2017.04.028.
- [78] B.C. De Cooman, K.O. Findley, Introduction to the mechanical behavior of steel, 2017.
- [79] R.H. Richman, G.F. Bolling, Stress, deformation, and martensitic transformation, Metall. Mater. Trans. B 2 (September) (1971) 2451–2462.
- [80] E. De Moor, S. Lacroix, A.J. Clarke, J. Penning, J.G. Speer, Effect of retained austenite stabilized via quench and partitioning on the strain hardening of martensitic steels, Metall. Mater. Trans. A 39 (11) (2008) 2586–2595, doi:10. 1007/s11661-008-9609-z.
- [81] K.W. Andrews, Empirical formulae for the calculation of some transformation temperatures, J. Iron Steel Inst. 203 (1965) 721–727.
- [82] J. Mola, G. Luan, Q. Huang, C. Ullrich, O. Volkova, Y. Estrin, Dynamic strain aging mechanisms in a metastable austenitic stainless steel, Acta Mater. 212 (2021) 116888, doi:10.1016/j.actamat.2021.116888.
- [83] E.J. Seo, L. Cho, B.C. De Cooman, Kinetics of the partitioning of carbon and substitutional alloying elements during quenching and partitioning (Q&P) processing of medium mn steel, Acta Mater. 107 (2016) 354–365, doi:10.1016/j. actamat.2016.01.059.
- [84] J. Speer, D.K. Matlock, B.C. De Cooman, J.G. Schroth, Carbon partitioning into austenite after martensite transformation, Acta Mater. 51 (9) (2003) 2611– 2622, doi:10.1016/S1359-6454(03)00059-4.
- [85] S. Yan, X. Liu, W.J. Liu, T. Liang, B. Zhang, L. Liu, Y. Zhao, Comparative study on microstructure and mechanical properties of a C-Mn-Si steel treated by quenching and partitioning (Q&P) processes after a full and intercritical austenitization, Mater. Sci. Eng., A 684 (December 2016) (2017) 261–269, doi:10.1016/j.msea.2016.12.026.
- [86] D.V. Edmonds, K. He, F.C. Rizzo, B.C. De Cooman, D.K. Matlock, J.G. Speer, Quenching and partitioning martensite-a novel steel heat treatment, Mater. Sci. Eng., A 438-440 (2006) 25-34, doi:10.1016/j.msea.2006.02.133.